



**ACTIVE AND ADAPTIVE CONTROL FOR PAYLOAD LAUNCH
VIBRATION ISOLATION**

THESIS

Julian R. Jarosh, Captain, USAF

AFIT/GA/ENY/00M-03

**DEPARTMENT OF THE AIR FORCE
AIR UNIVERSITY**

**AIR FORCE INSTITUTE OF
TECHNOLOGY**

Wright-Patterson Air Force Base, Ohio

APPROVED FOR PUBLIC RELEASE; DISTRIBUTION UNLIMITED

DHC QUALITY INSPECTED 4

20000803 133

The views expressed in this thesis are those of the author and do not reflect the official policy or position of the United States Air Force, Department of Defense or the U.S. Government.

AFIT/GA/ENY/00M-03

ACTIVE AND ADAPTIVE CONTROL FOR PAYLOAD LAUNCH
VIBRATION ISOLATION

THESIS

Presented to the Faculty
Department of Aeronautics and Astronautics
Graduate School of Engineering and Management
Air Force Institute of Technology
Air University
Air Education and Training Command
In Partial Fulfillment of the Requirements for
the Degree of Master of Science in Astronautical Engineering

Julian R. Jarosh, B.S., M.B.A

Captain, USAF

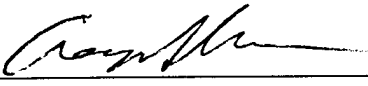
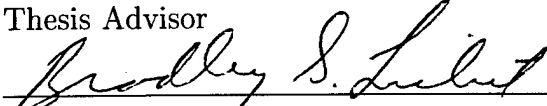
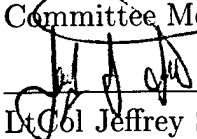
March 2000

Approved For Public Release; Distribution Unlimited

ACTIVE AND ADAPTIVE CONTROL FOR PAYLOAD LAUNCH
VIBRATION ISOLATION

Julian R. Jarosh, B.S., M.B.A
Captain, USAF

Approved:

	<u>09 Mar 00</u>
Captain Gregory S. Agnes, Ph.D Thesis Advisor	Date
	<u>09 Mar 00</u>
Dr. Bradley S. Liebst Committee Member	Date
	<u>09 Mar 00</u>
Dt Col Jeffrey S. Turcotte, Ph.D Committee Member	Date

Acknowledgements

First, I would like to thank my parents Roman and Martha whose devoted support shone through the pressures and questions of their own lives. I would also like to thank all of the GA-00M guys who always had time to listen to my opinions and helped ease the fleeting frustrations with laughs and good times. Thanks to Jen's sacrifices and her ability to share herself with my work on the outer circle. Thank you to Captain Greg Agnes who kept me motivated with his wisdom and insights into understanding and synthesizing my thesis work. Finally, I would like to thank the many excellent instructors here at AFIT. You taught me a lot about the subjects you needed to, but most of all that there is a bigger picture in research and learning. A picture that may have taken me a while to figure out, but I feel it was well worth the wait.

Julian R. Jarosh

Table of Contents

	Page
Acknowledgements	iii
List of Figures	vi
Abstract	x
I. Background and Statement of the Problem	1-1
1.1 Passive Vibration Isolation	1-2
1.2 Active Vibration Isolation	1-4
1.3 Adaptive Vibration Isolation	1-6
1.4 Organization of This Thesis	1-7
II. Literature Review	2-1
2.1 Passive Vibration Isolation	2-1
2.2 Active Vibration Isolation	2-1
2.3 Adaptive Vibration Isolation	2-3
2.4 Payload Launch Isolation	2-4
2.4.1 Passive Payload Launch Isolation	2-4
2.4.2 Active Payload Launch Isolation	2-5
III. Methodology	3-1
3.1 Equations of Motion	3-2
3.2 Passive Vibration Isolation	3-8
3.3 Active Vibration Isolation	3-10
3.3.1 PID Control	3-10
3.3.2 Skyhook Damper	3-12
3.4 Adaptive Vibration Isolation	3-15

	Page
IV. Data Description and Analysis	4-1
4.1 Full Run	4-1
4.2 Fixed Resonant Burn Frequency	4-3
4.2.1 Baseline Results	4-3
4.2.2 Passive Control Results	4-10
4.2.3 Active Control Results	4-13
4.2.4 Adaptive Control Results	4-22
4.3 Ramp Resonant Burn Frequency	4-29
4.3.1 Baseline Results	4-31
4.3.2 Passive Control Results	4-33
4.3.3 Active Control Results	4-35
4.3.4 Adaptive Control Results	4-41
V. Findings, Conclusions and Recommendations	5-1
5.1 Summary of Findings and Conclusions	5-1
5.2 Recommendations	5-2
Bibliography	BIB-1
Vita	VITA-1

List of Figures

Figure		Page
1.1.	Passive Vibration Isolation	1-2
1.2.	Passive Vibration Isolation: Displacement Transmissibility . .	1-4
1.3.	Active Vibration Isolation	1-5
1.4.	Active Vibration Isolation: Displacement Transmissibility [12]	1-5
1.5.	Adaptive Vibration Isolation	1-6
3.1.	Lumped Parameter System	3-1
3.2.	Passive Vibration Isolation Simulink Model [14]	3-9
3.3.	PID Hybrid Vibration Isolation Simulink Model [14]	3-11
3.4.	PID Controller Simulink Model [14]	3-12
3.5.	Skyhook Damper [7]	3-12
3.6.	Skyhook Damper Control Law	3-13
3.7.	Skyhook Damper Simulink Model	3-14
3.8.	Simulink Model Adaptation Laws and Adaptive Control Laws	3-20
4.1.	Launch Vehicle Mission Profile	4-2
4.2.	Full Run Payload Acceleration Profile	4-2
4.3.	Lower, Upper, and Inert Component Acceleration PSDs, Base- line Case	4-4
4.4.	Lower, Upper, and Inert Component Acceleration Spectrograms, Baseline Case	4-5
4.5.	Payload and Subcomponent Acceleration PSDs, Baseline Case	4-6
4.6.	Payload and Subcomponent Acceleration Spectrograms, Base- line Case	4-7
4.7.	Payload Effects of Varying Subcomponent Mass	4-8

Figure		Page
4.8.	Payload Effects of Varying Subcomponent Frequency	4-8
4.9.	Subcomponent Effects of Varying Subcomponent Frequency	4-9
4.10.	Subcomponent Effects of Varying Subcomponent Frequency	4-9
4.11.	Payload PSD, 27Hz Isolator	4-10
4.12.	Payload Spectrogram, 27Hz Isolator	4-11
4.13.	Subcomponent PSD, 27Hz Isolator	4-11
4.14.	Subcomponent Spectrogram, 27Hz Isolator	4-12
4.15.	Maximum Acceleration vs. Isolator Frequencies: Fixed Resonant Burn	4-13
4.16.	RMS Acceleration vs. Isolator Frequencies: Fixed Resonant Burn	4-14
4.17.	Active Control: Maximum Payload Acceleration vs. Isolator Frequencies, Fixed Resonant Burn	4-15
4.18.	Active Control: RMS Payload Acceleration vs. Isolator Frequencies, Fixed Resonant Burn	4-16
4.19.	PID Controller, 27 Hz Passive Isolator Inert Component, Payload, and Subcomponent Acceleration PSDs: Fixed Resonant Burn	4-17
4.20.	PID Controller, 40 Hz Passive Isolator Inert Component, Payload, and Subcomponent Acceleration PSDs: Fixed Resonant Burn	4-18
4.21.	Skyhook Damper, 27 Hz Passive Isolator Inert Component, Payload, and Subcomponent Acceleration PSDs: Fixed Resonant Burn	4-20
4.22.	Skyhook Damper, 40 Hz Passive Isolator Inert Component, Payload, and Subcomponent Acceleration PSDs: Fixed Resonant Burn	4-21
4.23.	Adaptive Control: Maximum Payload Acceleration vs. Isolator Frequencies, Fixed Resonant Burn	4-23
4.24.	Adaptive Control: RMS Payload Acceleration vs. Isolator Frequencies, Fixed Resonant Burn	4-24

Figure		Page
4.25.	Hybrid Control Effort: Fixed Resonant Burn	4-25
4.26.	Adaptive Control, 27 Hz Passive Isolator Inert Component, Payload, and Subcomponent Acceleration PSDs: Fixed Resonant Burn	4-27
4.27.	Adaptive Control, 40 Hz Passive Isolator Inert Component, Payload, and Subcomponent Acceleration PSDs: Fixed Resonant Burn	4-28
4.28.	Sample PSD: Ramp vs Fixed Resonant Burn	4-29
4.29.	Acceleration Spectrograms, Ramp Resonant Burn	4-30
4.30.	Lower Four Component Acceleration PSDs, Baseline Case: Ramp Resonant Burn	4-31
4.31.	Subcomponent Acceleration PSD, Baseline Case: Ramp Resonant Burn	4-32
4.32.	Maximum and RMS Accelerations: Ramp Resonant Burn	4-33
4.33.	Passive Isolation: 27 Hz Passive Isolator Payload and Subcomponent Acceleration PSDs: Fixed Resonant Burn	4-34
4.34.	Active Control: Maximum Acceleration vs. Isolator Frequencies, Ramp Resonant Burn	4-35
4.35.	Active Control: RMS Acceleration vs. Isolator Frequencies, Ramp Resonant Burn	4-36
4.36.	PID Control, 27 Hz Passive Isolator Inert Component, Payload, and Subcomponent Acceleration PSDs: Ramp Resonant Burn	4-37
4.37.	PID Control, 40 Hz Passive Isolator Inert Component, Payload, and Subcomponent Acceleration PSDs: Ramp Resonant Burn	4-38
4.38.	Skyhook Damper, 27 Hz Passive Isolator Inert Component, Payload, and Subcomponent Acceleration PSDs: Ramp Resonant Burn	4-39
4.39.	Skyhook Damper, 40 Hz Passive Isolator Inert Component, Payload, and Subcomponent Acceleration PSDs: Ramp Resonant Burn	4-40

Figure		Page
4.40.	Adaptive Control: Maximum Acceleration vs. Isolator Frequencies, Ramp Resonant Burn	4-41
4.41.	Adaptive Control: RMS Acceleration vs. Isolator Frequencies, Ramp Resonant Burn	4-42
4.42.	Hybrid Control Effort: Ramp Resonant Burn	4-43
4.43.	Adaptive Control, 27 Hz Passive Isolator Inert Component, Payload, and Subcomponent Acceleration PSDs: Ramp Resonant Burn	4-44
4.44.	Adaptive Control, 40 Hz Passive Isolator Inert Component, Payload, and Subcomponent Acceleration PSDs: Ramp Resonant Burn	4-45

Abstract

The Department of Defense has identified launch vibration isolation as a major research interest. Reducing the loads a satellite experiences during launch will greatly enhance the reliability and lifetime and decrease the payload structural mass. DoD space programs stand to benefit significantly from advances in vibration isolation technology.

This study explores potential hybrid vibration isolation using active and adaptive control with a passive isolator. The active control methods are Proportional-Integral-Derivative (PID) control and a skyhook damper. Lyapunov analysis is used to develop the structural adaptive control scheme. Simulink™ and Matlab™ simulations investigate these control methodologies on a lumped mass dynamic model of a satellite and its representative launch vehicle.

The results of the modeling indicate adaptive control achieves up to a 90 percent reduction in loads on the payload when compared to the conventional active control methods. The adaptive controller compensated for the loads being transmitted to the payload from the rest of the launch vehicle. The current adaptive controller was not able to effectively control the motion of a vibrating subcomponent within the payload or the subcomponent's effect on the overall payload itself.

ACTIVE AND ADAPTIVE CONTROL FOR PAYLOAD LAUNCH VIBRATION ISOLATION

I. Background and Statement of the Problem

The problem of vibration suppression or isolation is common to almost all industries. The automobile industry uses vibration isolation to increase ride comfort or to actively cancel out ride noise. The manufacturing industry uses it to dampen out unwanted machinery vibration in order to meet increasingly tighter tolerances. The aerospace industry uses it in a wide range of applications, including high cycle fatigue of turbine engines, damping structural vibrations, and isolating cargos and payloads from the harsh aerospace dynamic environment.

For space payloads, the vibration environment during launch is a major cause of satellite failure, especially upon orbit insertion. In fact, studies done by the National Aeronautics and Space Administration (NASA) Goddard Space Flight Center (GSFC) on 57 satellites launched from 1960-1970, identified this violent launch environment as the cause of 30-60 percent of first day satellite failures [31], [32]. This has spawned an extensive testing and design regimen to ensure a satellite's survivability during the intense vibrational environment of space launch. The testing and design effort accounts for a major portion of each satellite's cost and schedule [16], [30].

Recently, the Navy launched a GEOSAT Follow-on (GFO) satellite on an Air Force Taurus launch vehicle. Although the GFO was subjected to the strict testing

and design regimen of earlier satellites, it could not meet the specifications needed to survive a Taurus launch [13]. The Air Force Research Laboratory (AFRL) designed a payload vibration isolator that allowed the GFO to survive the Taurus launch environment, without having to redesign the satellite itself.

This thesis seeks to extend the work of Karahalidis [14] and the work currently being undertaken by AFRL to enhance whole spacecraft vibration isolation systems. It explores several methods of passive, active, and adaptive vibration isolation using Simulink™ and Matlab™ software packages. The vibration isolation methods are applied to the model developed by Karahalidis. This thesis focuses on the application of active and adaptive control laws to isolate a vibrating payload during launch.

1.1 *Passive Vibration Isolation*

Passive vibration isolation can be described using the aid of Figure 1.1 showing an object of mass M on top of a spring of stiffness K and a viscous damper with damping coefficient C . The base has some excitation displacement x_b . The base

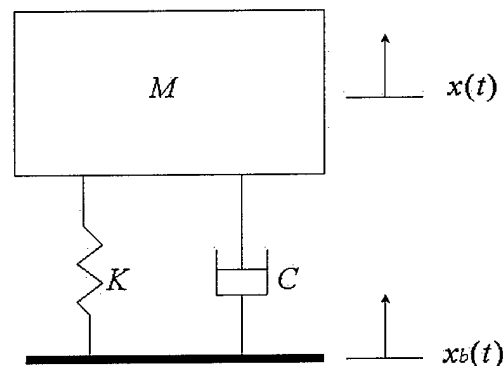


Figure 1.1 Passive Vibration Isolation

moves according to the nature of x_b , which is a function of time, and its velocity and acceleration are given by the displacement time derivatives, \dot{x}_b and \ddot{x}_b , respectively. For example, the base moves periodically if x_b is periodic with a frequency of ω . The object will also move according to the nature of x_b with a displacement, velocity, and acceleration of x , \dot{x} , and \ddot{x} , respectively. The equation of motion for this system is:

$$M\ddot{x} + C\dot{x} + Kx = Kx_b + C\dot{x}_b \quad (1.1)$$

The displacement transmitted from the excitation to the mass M depends on M , K , C , and x_b . If the natural frequency (ω_n) and damping ratio (ζ) of this system are defined as:

$$\omega_n = \sqrt{\frac{K}{M}} \quad (1.2)$$

and

$$\zeta = C/C_{cr} \quad (1.3)$$

where

$$C_{cr} = 2\sqrt{KM}$$

then, using equations 1.1, 1.2, and 1.3, it can be found that:

$$|x/x_b| = \frac{\sqrt{1 + (2\zeta\omega/\omega_n)^2}}{\sqrt{[1 - (\omega/\omega_n)^2]^2 + (2\zeta\omega/\omega_n)^2}} \quad (1.4)$$

Where $|x/x_b|$ is defined as the *displacement transmissibility* [12] and measures the magnitude of the displacement of the object compared to the magnitude of the displacement of the base. Figure 1.2 shows the displacement transmissibility ($X/Y = |x/x_b|$) over a range of normalized frequencies (ω/ω_n) for a passively isolated SDOF system. The key to passive vibration isolation is to choose K and C to transmit as little of the excitation displacement, x_b , as possible to the mass, M , and to obtain a desirable resonant response. The mass is isolated when $(\omega/\omega_n) > \sqrt{2}$ for a low damping ratio, ζ . In this frequency range, the displacement transmitted to M will

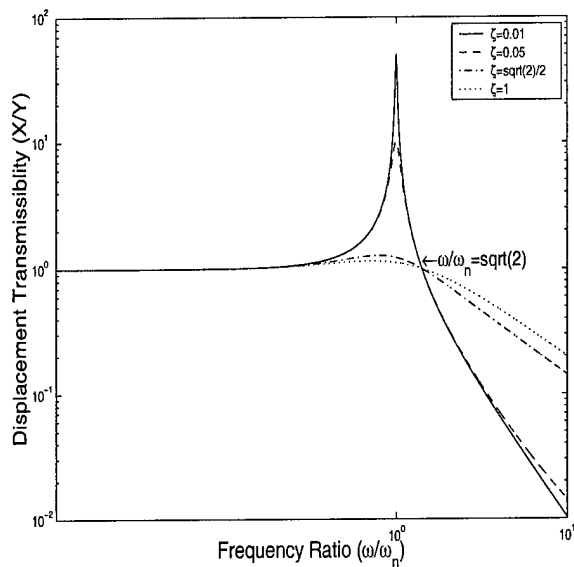


Figure 1.2 Passive Vibration Isolation: Displacement Transmissibility

always be less than x_b . Therefore, K must be chosen such that $(\omega/\omega_n) > \sqrt{2}$. Also, C must be chosen in order to obtain a desirable resonant response. Resonance occurs when $(\omega/\omega_n) \approx 1$. Choosing a desirable ζ and thus C means adding damping to the system. Damping, however, increases the amount of displacement transmitted to M in the region $(\omega/\omega_n) > \sqrt{2}$, while decreasing the resonant response (when $(\omega/\omega_n) \approx 1$).

1.2 Active Vibration Isolation

Active vibration isolation involves the addition of an actuator force, f_a , to counterbalance the effect of the transmitted displacement, x , of the object, as shown in Figure 1.3. The key in active vibration isolation is to choose f_a such that $x < x_b$ when $(\omega/\omega_n) > \sqrt{2}$ and to achieve a desired resonant response when $(\omega/\omega_n) \approx 1$. The nature and magnitude of f_a depends on the nature and magnitude of x_b and on the characteristics of the system itself (M , K , C , and x). The advantage of active vibration isolation is that f_a can be chosen in such a manner that increasing system damping does not necessarily mean decreased isolation when $(\omega/\omega_n) > 1$ [15]. Figure

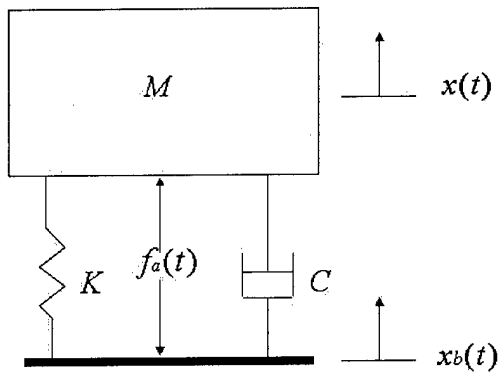


Figure 1.3 Active Vibration Isolation

1.4 shows the displacement transmissibility of an actively isolated SDOF system with respect to a non-dimensionalized frequency, $\Omega = (\omega/\omega_n)$. $W_R(j\omega)$ is defined as the

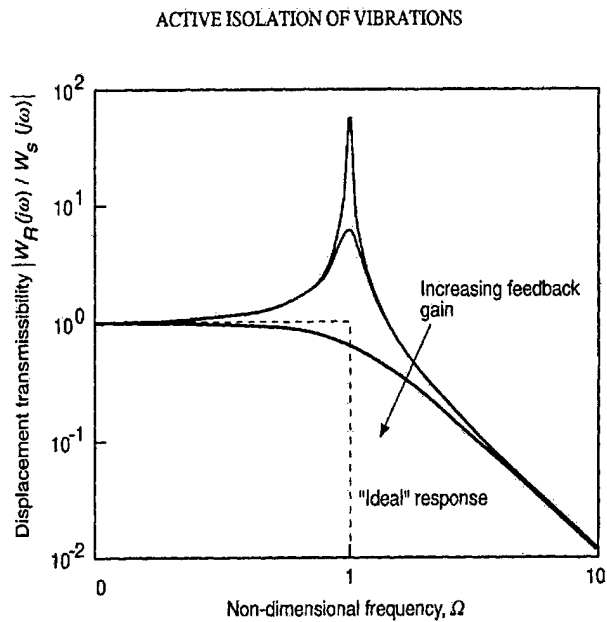


Figure 1.4 Active Vibration Isolation: Displacement Transmissibility [12]

magnitude of the displacement frequency response of the system (analogous to x in

Section 1.1), and $W_S(j\omega)$ is defined as the magnitude of the displacement frequency response of the excitation (analogous to x_b in Section 1.1).

Usually f_a is chosen through the use of a sensor that can detect one or more of the states x , \dot{x} , or \ddot{x} . The state or states can then be fed back to a controller. A controller, collocated with the sensor, formulates an output to the actuator through a set of control laws. Based on the output of the controller, the actuator then applies f_a .

1.3 Adaptive Vibration Isolation

Adaptive isolation is needed if the system itself is changing with respect to time. For example, in Figure 1.5, the object is continually losing mass over time (\dot{M}_{out}). In this case, w_n is either unknown or drifting, and f_a needs to adapt in order to account for this [11].

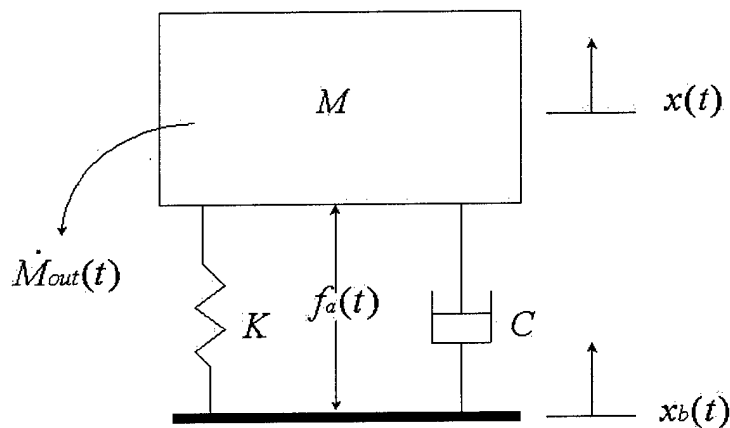


Figure 1.5 Adaptive Vibration Isolation

These three vibration isolation schemes form the basis for this thesis. Each scheme presents its own benefits and disadvantages. The goal of this thesis is to explore how each of these vibration isolation methodologies affect the loads a payload experiences during space launch.

1.4 Organization of This Thesis

This thesis is organized into five chapters. This chapter presented background on the vibration isolation problem. The second presents a literature review of passive, active, and adaptive vibration isolation and applies them to the whole spacecraft vibration isolation problem. The third reviews the equations of motion of a five-degree of freedom (5-DOF) rocket model, the Simulink™ model used to represent it, and the control methodologies used to isolate the payload in the model. The fourth chapter presents the results of the different control methodologies, and the fifth chapter summarizes findings and conclusions and gives recommendations for future research.

II. Literature Review

Industry has used passive isolation for nearly a century to reduce high frequency disturbances in a myriad of applications [12], [15], [17], [19], [26]. Active isolation has shown promise mostly for noise control, vibrating machinery [8], [15], [18], [26], [27], [28], [33] and control of large structures [9], [22], [29], and is being applied to a number of other industrial applications to include spacecraft vibration isolation [1], [2], [3], [7], [13], [14], [17], [23], [25], [26], [27]. Adaptive vibration isolation is used when the nature of a disturbance force or the properties of the disturbed system are changing or unknown [4], [5], [10], [11], [20], [26], [33].

2.1 Passive Vibration Isolation

Passive vibration isolation covers a broad spectrum of engineering problems. It usually results in good high frequency vibration attenuation, but design for localized mode attenuation may actually produce poor high frequency results, as shown in Section 1.1. For more information, reference Inman [12] or Meirovitch [19].

2.2 Active Vibration Isolation

For most industrial and defense applications, passive vibration isolation works well for high frequency effects; however, active vibration isolation shows considerable advantages in the low frequency realm [8]. Multiple research efforts [14], [18], [28] using active vibration isolation on structures and experiments other than spacecraft, note that there is an interaction between passive and active vibration isolation. When an object to be isolated is mounted on a passive structure, active isolation interacts with characteristics of that object's mount.

Mangiante and Roure [18] developed a Noise and Vibration Active Control System (NOVACS) to test its effects on tire-road automobile noise, aircraft cabin noise, and cancellation of axial mechanical vibrations from a diesel engine. The NOVACS used a multiple-input, multiple-output (MIMO) least-mean-squares (LMS) control algorithm. Of particular note was an attenuation of up to 30 decibels (dB) in the acceleration spectrum of the axial mechanical vibrations from a diesel engine.

Burdisso and Heilmann [2] explored the effects of a dual-reaction mass dynamic vibration absorber (DM-DVA) for active vibration control. The DM-DVA is similar in configuration to Figure 1.3, however instead of isolating the primary mass M , Burdisso and Heilmann sought to isolate the base using the mass, M , as a vibration absorber. In addition, they used two vibration absorbing masses rather than one; as would be the case in a single-reaction mass dynamic vibration absorber (SM-DVA). The DM-DVA uses two masses mounted on top of a spring and viscous damper with a controlling force between the two masses. Using the LMS control algorithm applied to a lumped SDOF system, they were able to show transmissibility reductions of up to a factor of 11.5 for a free-fixed beam and the superiority of the DM-DVA over the SM-DVA in terms of response reduction and greater control authority.

Sievers and von Flotow present optimal and Linear Quadratic Gaussian (LQG) active control for machinery mounts [26]. This work focuses mostly on narrow-band isolation with known flexible machine frequency response. Later, Sievers, von Flotow, and Scribner applied active control to a lightly damped flexible structure with unknown frequency response [28]. They found tradeoffs between controller stability and robustness for modally sparse structures.

In line with the work done by Sievers, von Flotow and Scribner for vibrating machinery, Sciulli [23] found that the active isolator is also affected by the stiffness of the machinery mount. Using Proportional-Integral-Derivative (PID), LQG, and Positive Position Feedback (PPF) control, he showed a definite dependence between the amount of isolation you can get from an active isolator and the stiffness of the

machine mount. In fact, depending on the natural frequency of the mount, one can make several tradeoffs in terms of which frequencies are affected by the active isolator.

2.3 Adaptive Vibration Isolation

Sievers and von Flotow [27] present active and adaptive control as applied to narrow-band disturbance rejection. Using some modifications of the LMS adaptive feedforward methodology, they were able to solve for a control algorithm that is not only robust in frequency response, but can also be effective over fast-moving and slow-moving states in the time domain. These results were also recognized by von Flotow for possible use in isolating vibrating machines [33].

Elliott, *et al* [4] present a generalized filtered- x LMS algorithm for vibrating or rotating machines with a known periodic disturbance. Frequency and time domain analysis showed the adaptive convergence through the use of digital filters. The study focused on sound vibration and adaptively controlling error to reduce noise.

Guigou, *et al* [10] used a feedforward filtered- x LMS algorithm to show adaptive isolation using an adaptive structure. They used an experiment with a thick plate simulating a vibrating machine mounted on springs. The springs were attached to an adaptive thin elastic steel plate configured with piezoelectric actuators. They showed that the placement of the sensors and actuators can have a dramatic effect on the isolation of the simulated vibrating machine.

Hillerström [11] showed that using a gradient descent adaptation law may prove difficult because of the problem of choosing a step length which determines convergence speed. To obtain better results than the gradient descent law, he used a Newton method. The Newton method impaired stability robustness but improved the adaptation scheme. The Newton Method's adaptation scheme was easier to tune and converged more quickly than the gradient descent law.

Queiroz, *et al* [20] present a continuous system approach to adaptive vibration isolation as applied to axial vibrations in a string. Their objective was to drive string vibration to zero using Lyapunov techniques. By being able to measure certain states of the string, an actuator adapted to a variety of arbitrary inputs to reduce its vibration.

Ertur, *et al* [5] applied the work of Queiroz, *et al* [20] to flexible structures in the form of lumped parameter systems. Again, using Lyapunov techniques, they showed that a system can be adaptively controlled and can successfully track state errors. An experimental verification using a 3-DOF system showed improvements over traditional active techniques.

2.4 Payload Launch Isolation

Until recent development in lightweight actuator/sensor technology, most spacecraft launch isolation research has focused on passive methods. Although passive methods work well, their effects are generally untested over a wide range of launch environments or launch vehicles. Active isolation methods present an advantage by providing a lighter, albeit more complex isolator. However, most widely known methods of active control (such as LQG, H- ∞ , or optimal control) focus on coming up with an optimal mix of pole locations rather than focusing on isolating one or two dominant modes. Neither passive nor active methods allow for satisfactory robustness in a time varying system. In the case of space launch, the characteristics of the launch vehicle/payload system change drastically as propellant is used and stages are expelled. This drives the need for research in the area of adaptive vibration isolation for spacecraft mounted on a launch vehicle.

2.4.1 Passive Payload Launch Isolation. On 10 Feb 98, a passive whole-spacecraft vibration isolation system was flown on the Taurus launch vehicle carrying the Navy GFO satellite. CSA Engineering in conjunction with

AFRL designed the vibration isolation system [13]. The isolation system reduced axial/lateral acceleration loading by up to 88%. CSA used a finite element model for the isolator design and a four DOF model to study different isolator effects. In the four DOF model, three degrees of freedom modeled the launch vehicle and one degree of freedom modeled the payload. The favorable results of this research called for further use of this passive vibration isolator on future GFO/Taurus launches.

2.4.2 Active Payload Launch Isolation. Research done by Argento [1] used a finite element model of a satellite to determine the mode shapes and frequencies of a payload during launch. The results from the finite element model were then compared to those of a beam under active and passive isolation. Argento was able to closely match the modal characteristics of the satellite finite element model to those of the beam. Next, Argento applied passive vibration isolation using viscoelastic material and active vibration isolation using proportional gain Single-Input-Single-Output (SISO) and Multiple-Input-Multiple-Output (MIMO) feedback. Using several isolator configurations, it was found that the passive isolation was able to provide more damping to the vibrating beam than the proportional feedback schemes.

Glauser, Ahmadi, and Layton [17] used a five DOF lumped parameter model of the Space Transportation System (STS) to develop passive and active vibration isolation strategies. They chose to explore the active vibration absorber (AVA) for their active control law. They noted that the AVA did not have a significant effect on the high frequency vibrations of liftoff but was able to significantly suppress specific vibration modes.

In 1997, Phillips Lab [3] studied LQR, LQG and optimal active control for launch vibration isolation using a specially designed Payload Attached Fitting and a Cold Gas Hydraulic Blowdown System. The study found that active control could essentially zero out some transient vibrations on the payload and reduce the effects of

lift-off and engine cut-off impulses. This could be done with relatively small control force requirements, using velocity and acceleration feedback rather than position feedback.

Using the passive isolation system developed by CSA Engineering, AFRL [24] designed and built an experimental testbed for a combination of passive/active spacecraft vibration isolation. Known as a hybrid launch isolation system, AFRL used the CSA passive isolator and four piezoceramic actuators to perform the active part of the isolation. Although not tested to the extremes of the actual launch environment, this experiment found possible significant loading reduction on the payload versus the passive-only system. Also, the launch vehicle stiffness could play a major role in determining how to implement active control laws.

Karahalis [14] used a five DOF model to perform research on a hybrid whole-spacecraft vibration isolator. The active part of the hybrid isolator used PID or PPF control. This research showed a possible 10% improvement in isolator performance over a passive-only system as well as a 90% improvement over a non-isolated system. There was also evidence of a dependence of active isolation on the critical frequency of the passive isolator. This is similar to the results obtained by Sciulli [23]. Karahalis' work showed that the PPF isolator introduces substantial steady-state error, while the PID isolator did not introduce steady-state error. The addition of a DOF for a payload subcomponent showed that while hybrid control may decrease loading for the payload, the subcomponent may be subject to increased loading.

Much of the research for whole-spacecraft active vibration isolation has shown a possible need for an active/passive hybrid isolator. There will be several low frequency modes, an interaction of the base isolator with the active controller, and a need for a good transient response for lift-off and staging events.

The literature for launch vibration isolation begins with the basic isolation problem and extends through to applying passive and active isolation methods to isolate the launch payload. Research shows that passive isolation greatly reduces

payload vibrations, while active isolation needs further study. Research for adaptive vibration isolation focuses on noise rejection, though recent advances in methods of adaptive isolation allow for a structural view for modal control.

III. Methodology

The rocket model used for analysis of vibration isolation is a five-degree-of-freedom (5-DOF) lumped parameter system, as shown in Figure 3.1, with stiffness and damping values between each mass. Only the axial motion of the rocket is taken into

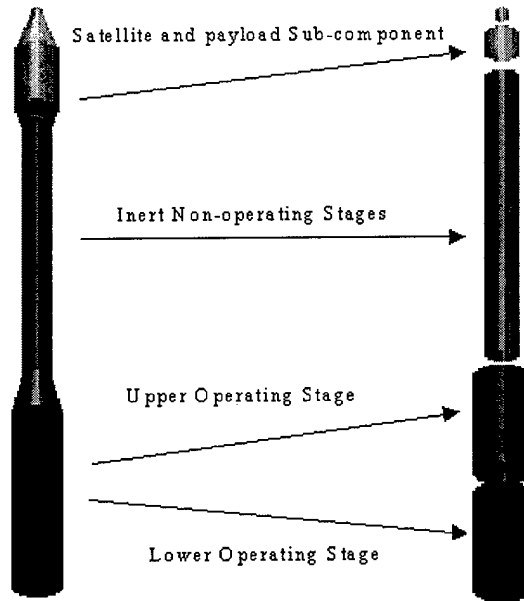


Figure 3.1 Lumped Parameter System

account. The forces acting on the rocket are thrust, drag, gravity, motor noise, aeroacoustic noise, and, in the case of active and adaptive control, the isolator force. The equations of motion are presented in both mass-spring-damper (M-K-C) form [19] and in the state space representation [6]. The forces, equations of motion, and vibration isolation strategies are then incorporated into a Simulink™ model as outlined in the following sections.

3.1 Equations of Motion

The 5-DOF model represents five masses interconnected with springs and dampers. The first and fifth masses are free on one side. The launch vehicle is divided into lower (L), upper (U) and inert (I) components. The lower and upper components are the operating stages of the launch vehicle and exhibit the effects of variable mass as the launch vehicle expends fuel. The inert component accounts for the remaining stages of the launch vehicle that are not expended. The remaining two degrees of freedom are the payload component and the payload subcomponent denoted as (P) and (1), respectively. The subcomponent simulates a mass of interest within the payload. Gravity turn equations as presented in Karahalis [14] model the launch vehicle's center of gravity dynamics.

The following presentation of the M-K-C form is modified from the discussion presented in Meirovitch [19]. Using the equation:

$$M\ddot{x} + C\dot{x} + Kx = B_f F \quad [19] \quad (3.1)$$

Where M , K and C are the mass, stiffness coefficient, and damping coefficient matrices of the 5-DOF launch vehicle, B_f is a force coefficient matrix and

$$x = \left[X_L \quad X_U \quad X_I \quad X_P \quad X_1 \right]^T$$

the displacements of the lower component, upper component, inert component, payload component and subcomponent, respectively. The force vector, F is:

$$F = \left[T \quad N_M \quad N_A \quad D \quad I_c \right]^T$$

where:

T = thrust

N_M = motor noise

N_A = aero-acoustic noise

D = drag

I_c = isolator control force

The methodology for calculating T , N_M , N_A , and D can be found in Karahalis [14]. Thrust and aero-acoustic noise are essentially scaled random noise, motor noise is a tuned vibration, and drag is dependent upon altitude and atmospheric pressure. The motor noise and aero-acoustic noise are the primary causes of payload vibration. A major component of motor noise is resonant burn. Resonant burn occurs when the combustion cavity and mass flow rate create a resonance. The vibrations cause an oscillation of the propellant remaining in the motor [14]. Aero-acoustic noise is scaled based on the dynamic pressure encountered by the launch vehicle throughout its flight. The maximum dynamic pressure, or max-q, occurs at 27 seconds after liftoff, which is during the first stage firing [14].

The mass matrix for the model is:

$$M = \begin{bmatrix} M_L & 0 & 0 & 0 & 0 \\ 0 & M_U & 0 & 0 & 0 \\ 0 & 0 & M_I & 0 & 0 \\ 0 & 0 & 0 & M_P & 0 \\ 0 & 0 & 0 & 0 & M_1 \end{bmatrix}$$

with the masses taking on the following values at liftoff (in kg):

$$M_L = 26,908$$

$$M_U = 26,112$$

$$M_I = 18,580$$

$$M_P = 1,780 (1,730 \text{ kg} + M_1)$$

$$M_1 = 50$$

These values are representative of a generic launch vehicle. The total mass (M_G) is:

$$M_G = M_L + M_U + M_I + M_P + M_1$$

The values for M_L and M_U vary as fuel is expended, the value for M_I varies as launch vehicle stages are jettisoned but remains constant for a single stage's flight, and the values for M_P and M_1 are constant throughout the duration of flight. The time rate of change of mass in the first stage is $\dot{M}_L = \dot{M}_U = -299.417 \text{ kg/s}$.

The stiffness matrix is:

$$K = \begin{bmatrix} k_{LU} & -k_{LU} & 0 & 0 & 0 \\ -k_{LU} & k_{LU} + k_{UI} & -k_{UI} & 0 & 0 \\ 0 & -k_{UI} & k_{UI} + k_{IP} & -k_{IP} & 0 \\ 0 & 0 & -k_{IP} & k_{IP} + k_{P1} & -k_{P1} \\ 0 & 0 & 0 & -k_{P1} & k_{P1} \end{bmatrix}$$

where k_{ij} is the stiffness coefficient between the i^{th} and j^{th} component. The values for k_{ij} are representative of a generic launch vehicle and are (in N/m):

$$\begin{aligned} k_{LU} &= 4 \cdot 10^8 \\ k_{UI} &= 1 \cdot 10^8 \\ k_{IP} &= M_P \cdot (2\pi \cdot \omega_P)^2 \\ k_{P1} &= M_1 \cdot (2\pi \cdot \omega_1)^2 \end{aligned}$$

The values for k_{IP} and k_{P1} allow us to tune the isolator and subcomponent to a desired frequency. The value of ω_P (the payload component frequency) gives the isolator frequency and the value of ω_1 (the subcomponent component frequency) gives the subcomponent undamped natural frequency. For the baseline case, $\omega_P = 200$ Hz, simulating a hardmounted payload. For the passive isolation and hybrid (passive isolation with active or adaptive control) cases, ω_P varies from 25 to 40 Hz. In all cases, ω_1 is tuned to 50 Hz.

The damping matrix is:

$$C = \begin{bmatrix} c_{LU} & -c_{LU} & 0 & 0 & 0 \\ -c_{LU} & c_{LU} + c_{UI} & -c_{UI} & 0 & 0 \\ 0 & -c_{UI} & c_{UI} + c_{IP} & -c_{IP} & 0 \\ 0 & 0 & -c_{IP} & c_{IP} + c_{P1} & -c_{P1} \\ 0 & 0 & 0 & -c_{P1} & c_{P1} \end{bmatrix}$$

where c_{ij} is the damping coefficient between the i^{th} and j^{th} component. The values for c_{ij} are representative of a generic launch vehicle and are (in N-s/m):

$$\begin{aligned} c_{LU} &= 90 \cdot 10^3 \\ c_{UI} &= 45 \cdot 10^3 \\ c_{IP} &= M_P \cdot (2 \cdot \zeta_P \cdot \omega_P) \cdot 2\pi \\ c_{P1} &= M_1 \cdot (2 \cdot \zeta_1 \cdot \omega_1) \cdot 2\pi \end{aligned}$$

where ζ_P and ζ_1 are the component damping ratios between the payload and inert component and between the subcomponent and payload, respectively. In the model, these values are both set at $\zeta_P = \zeta_1 = 0.01$. The component frequencies (ω_i) and component damping ratios (ζ_i) are not modal frequencies or modal damping ratios. They are the natural frequencies and damping ratios obtained for each component as if it were a single degree of freedom.

The forcing matrix, B_f , becomes:

$$B_f = \begin{bmatrix} 1 - \frac{M_L}{M_G} & 1 - \frac{M_L}{M_G} & -\frac{M_L}{M_G} & \frac{M_L}{M_G} & 0 \\ -\frac{M_U}{M_G} & -\frac{M_U}{M_G} & -\frac{M_U}{M_G} & \frac{M_U}{M_G} & 0 \\ -\frac{M_I}{M_G} & -\frac{M_I}{M_G} & 1 - \frac{M_I}{M_G} & \frac{M_I}{M_G} - 1 & -1 \\ -\frac{M_P}{M_G} & -\frac{M_P}{M_G} & -\frac{M_P}{M_G} & \frac{M_I}{M_P} & 1 \\ -\frac{M_1}{M_G} & -\frac{M_1}{M_G} & -\frac{M_1}{M_G} & \frac{M_1}{M_G} & 0 \end{bmatrix}$$

where thrust and motor noise are the only external forces on the lower component while aero-acoustic noise and drag act on the inert component. The isolator control force acts in opposite senses on the inert component and payload.

The following presentation of the state-space form is modified from the discussion presented in Fuller, *et al* [7]. To put this model into state-space representation, a state vector, X is defined:

$$X = \left[X_L \quad X_U \quad X_I \quad X_P \quad X_1 \quad \dot{X}_L \quad \dot{X}_U \quad \dot{X}_I \quad \dot{X}_P \quad \dot{X}_1 \right]^T$$

X has dimension n . The state-space representation from Franklin, *et al* is:

$$\begin{aligned} \dot{X} &= AX + Bu \\ y &= C_{ss}X + Du \end{aligned} \quad [6] \quad (3.2)$$

where u is the input force matrix and:

$$\dot{X} = \left[\dot{X}_L \quad \dot{X}_U \quad \dot{X}_I \quad \dot{X}_P \quad \dot{X}_1 \quad \ddot{X}_L \quad \ddot{X}_U \quad \ddot{X}_I \quad \ddot{X}_P \quad \ddot{X}_1 \right]^T$$

A has dimension $n \times n$, u has dimension $l \times 1$ (where there are l inputs), B has dimension $n \times l$, C_{ss} has dimension $m \times n$ (where m is the number of outputs) and D has dimension $m \times l$ [21]. In the case of the 5-DOF rocket:

$n = 10$, the 10 states of X

$l = 2 \cdot 5 = 10$, the 5 elements of F

$m = 10$, all 10 states are observable

To put the previous M-K-C form into state space, the A , B , C_{ss} and D matrices are chosen such that:

$$A = \begin{bmatrix} [0] & [I] \\ -M^{-1}K & -M^{-1}C \end{bmatrix} \quad B = \begin{bmatrix} [0] \\ -M^{-1}B_f \end{bmatrix} \quad [12]$$

$$C_{ss} = \begin{bmatrix} [C_p] & [0] \\ [0] & [C_v] \end{bmatrix} \quad D = [0] \text{ or acceleration feed-through terms} \quad (3.3)$$

where $[I]$ is the identity matrix, and $[0]$ is a null matrix of appropriate dimension. The matrices $[C_p]$ and $[C_v]$ are weighting coefficient matrices on position and velocity, respectively. In the case of only choosing payload and subcomponent position and

velocity as outputs:

$$C_{ss} = \begin{bmatrix} [C_p] & [0] \\ [0] & [C_v] \end{bmatrix} = \begin{bmatrix} \begin{bmatrix} 0 & 0 & 0 & 0 & 0 \\ 0 & 0 & 0 & 0 & 0 \\ 0 & 0 & 0 & 0 & 0 \\ 0 & 0 & 0 & 1 & 0 \\ 0 & 0 & 0 & 0 & 1 \\ 0 & 0 & 0 & 0 & 0 \\ 0 & 0 & 0 & 0 & 0 \\ 0 & 0 & 0 & 0 & 0 \\ 0 & 0 & 0 & 0 & 0 \\ 0 & 0 & 0 & 0 & 0 \end{bmatrix} & \begin{bmatrix} 0 & 0 & 0 & 0 & 0 \\ 0 & 0 & 0 & 0 & 0 \\ 0 & 0 & 0 & 0 & 0 \\ 0 & 0 & 0 & 0 & 0 \\ 0 & 0 & 0 & 0 & 0 \\ 0 & 0 & 0 & 0 & 0 \\ 0 & 0 & 0 & 0 & 0 \\ 0 & 0 & 0 & 0 & 0 \\ 0 & 0 & 0 & 1 & 0 \\ 0 & 0 & 0 & 0 & 1 \end{bmatrix} \end{bmatrix}$$

3.2 *Passive Vibration Isolation*

To run the model for passive vibration isolation, the equations of motion in M-K-C form and the force calculations are entered into Simulink™. Figure 3.2 shows the Simulink™ model for the passive vibration isolation case.

The equations of motion are in the Vibration Dynamics mask and the B_f matrix is in the Axial Forcing Functions mask. The gravity turn equations are in the Launch Vehicle Center of Gravity (LV CG) Dynamics mask. The gravity turn equations drive the direction of thrust and account for the velocity of the center of gravity as fuel is expended. The noise generator creates the vibration environment (motor noise and aero-acoustic noise) as filtered random signals.

Active and adaptive vibration isolation use the same Simulink™ model as passive isolation. The differences with the hybrid isolation schemes fall in the implementation of their respective control laws for the Simulink™ model. The following sections discuss their implementation.

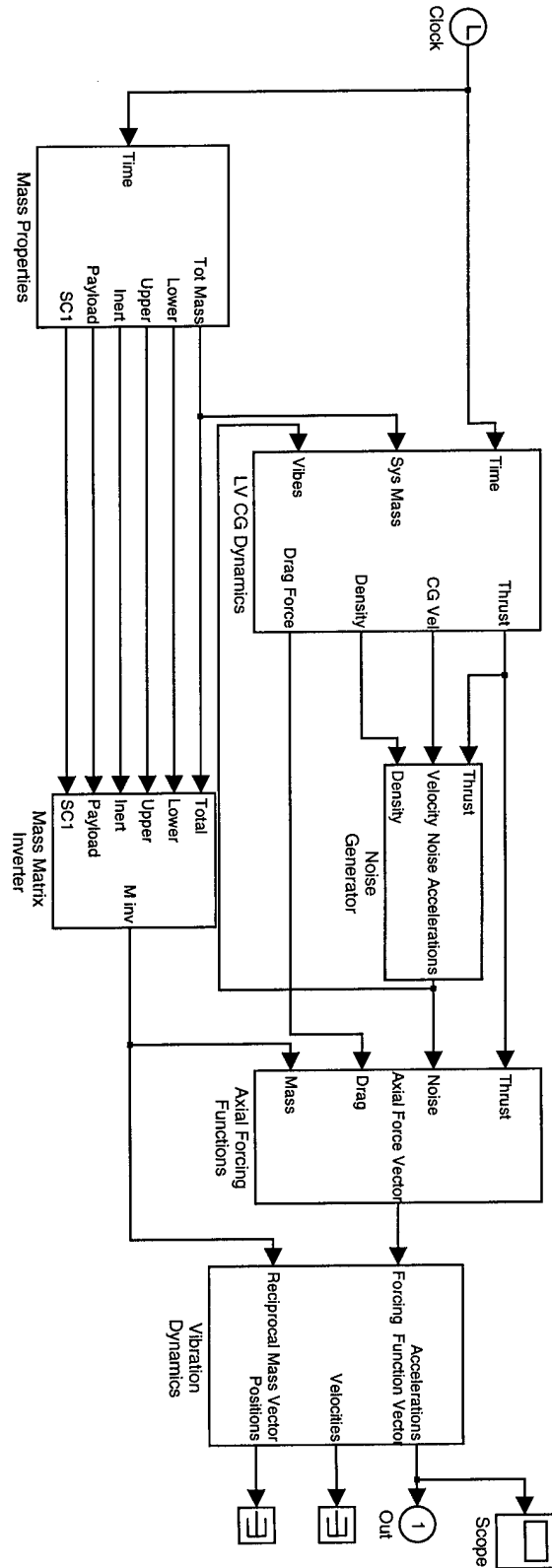


Figure 3.2 Passive Vibration Isolation Simulink Model [14]

3.3 Active Vibration Isolation

3.3.1 PID Control. Proportional-Integral-Derivative control uses a state feedback strategy by inputting a state output value from the state-space representation of the 5-DOF rocket into a controller. The controller then integrates, differentiates, and multiplies the state output and feeds the sum of these values back into the state-space model of the system. In the Laplace domain, the transfer function of the controller is [6]:

$$G(s) = K_p + \frac{K_I}{s} + K_D s \quad (3.4)$$

The differentiator's Laplace domain representation is s , and the integrator's Laplace domain representation is $1/s$. K_P , K_D and K_I are the proportional, derivative, and integral gains, respectively. The model uses the following gain values:

$$K_P = 5 \cdot 10^{-10}$$

$$K_I = 3 \cdot 10^{-10}$$

$$K_D = 8 \cdot 10^{-11}$$

Figure 3.3 shows the Simulink™ model for the 5-DOF rocket with hybrid passive and PID vibration isolation.

The values for K_P , K_I , and K_D are entered into the PID controller mask - see Figure 3.4. Payload acceleration (\ddot{X}_p) is fed back from the output of Vibration Dynamics and into the Axial Forcing Function mask. There, the control force (I_c) is added to the force on the inert component and subtracted from the force on the payload (negative feedback). The skyhook damper also uses a negative feedback scheme but feeds back velocity rather than acceleration.

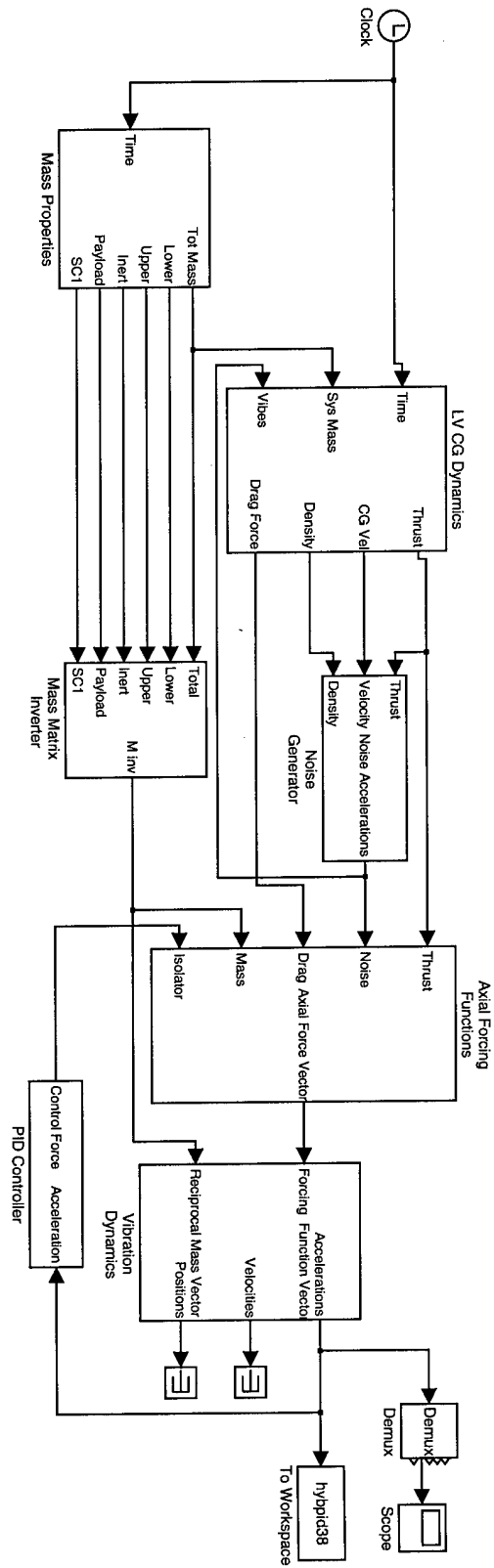


Figure 3.3 PID Hybrid Vibration Isolation Simulink Model [14]

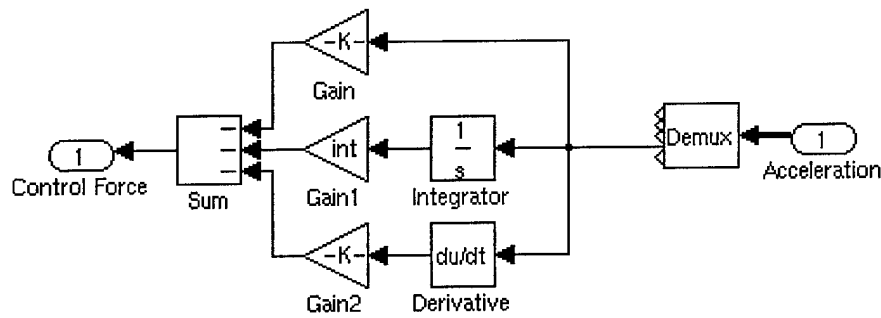


Figure 3.4 PID Controller Simulink Model [14]

3.3.2 Skyhook Damper. The principal of a skyhook damper is presented by Fuller, *et al* [7]. Figure 1.4 in Section 1.2 was generated for a 1-DOF spring-mass-damper system using skyhook damper active control. Adding a skyhook damper is essentially the same as adding a passive damper that is attached to an inertial point between a vibrating mass and its base - see Figure 3.5 below. In Figure 3.5, W_S is the Laplace transform of the displacement of the source of vibrations, f_s is the actuator force, and W_R is the Laplace transform of the displacement of the mass, M . The main difference with the 5-DOF rocket model, is that the payload is not resting on an inertial base but on the inert component, which is actually connected to the payload with a stiff spring and a light damper. Therefore, some of the control force will be transmitted to the inert component and to the lower components of the launch vehicle.

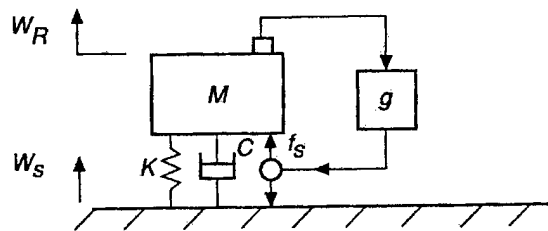


Figure 3.5 Skyhook Damper [7]

In the Simulink™ model, the payload velocity is fed back from the output of Vibration Dynamics and into the Axial Forcing Function mask. The control force obeys the control law:

$$I_c = -g\dot{X}_P$$

where

$$g = 2\zeta_c\omega_P$$

to effectively reduce the passive isolator resonant response at ω_P . The value for ζ_c is loosely called the damping ratio of the controller. The controller is not a mass-damper system, however it is convenient to treat it as one. In the Simulink™ model ζ_c is chosen to be 100 in order to effectively maximize the amount of resonance reduction while not causing the system to go unstable due to too much force being transmitted from the controller to the inert component, and thus the rest of the rocket. Figure 3.6 shows the skyhook damper control law where Gain 1 is $2\zeta_c\omega_P$.

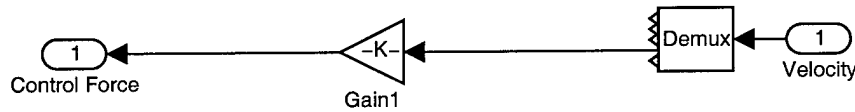


Figure 3.6 Skyhook Damper Control Law

The Simulink™ model is shown in Figure 3.7. The skyhook damper also uses a proportional feedback gain:

$$K_p = 5 \cdot 10^{-10}$$

The PID controller and skyhook damper feed acceleration or velocity, conditioned by a control law, back to an active isolator. The adaptive vibration isolator takes the positions and velocities of different components of the launch vehicle and forms an adaptive control law that reacts to the rate of change of the positions and velocities. While the PID controller and skyhook damper are essentially gain-driven proportional feedback, the adaptive controller adjusts its feedback gains to cancel out vibrations driving the payload.

3.4 Adaptive Vibration Isolation

The adaptive control law used in this model is taken from Ertur, *et al* [5]. In order to implement this control law, equation 3.1 must be rewritten:

$$M\ddot{q} + C\dot{q} + Kq = f \quad (3.5)$$

where q are the physical coordinates, and M , K , and C are again the mass, stiffness coefficient, and damping coefficient matrices, respectively. The force vector f is made up of the force inputs to each degree of freedom.

The M , K and C matrices must be rearranged in order to be partitioned into controllable and uncontrollable parts:

$$M = \begin{bmatrix} M_c & 0 \\ 0 & M_u \end{bmatrix} \quad (3.6)$$

$$C = \begin{bmatrix} D_c & D_{cu} \\ D_{uc} & D_u \end{bmatrix} \quad (3.7)$$

$$K = \begin{bmatrix} K_c & K_{cu} \\ K_{uc} & K_u \end{bmatrix} \quad (3.8)$$

where the subscript c denotes the controllable part, u denotes the uncontrollable part, and cu and uc denote cross terms. The vector f is partitioned into unknown disturbance inputs (subscript u) and forces onto controllable degrees of freedom (subscript c) such that:

$$f = [f_c, f_u]^T$$

Now equation 3.5 can be split into a controlled coordinates equation of motion:

$$M_c\ddot{q}_c + C_c\dot{q}_c + K_cq_c = -K_{cu}q_u - C_{cu}\dot{q}_u + f_c \quad (3.9)$$

and an uncontrolled coordinates equation of motion:

$$M_u \ddot{q}_u + C_u \dot{q}_u + K_u q_u = -K_{uc} q_c - C_{uc} \dot{q}_c + f_u \quad (3.10)$$

In order to regulate the controlled states, equation 3.9 is rewritten:

$$M_c \ddot{q}_c + C_c \dot{q}_c + K_c q_c = -Y_r \Phi_r + f_c \quad (3.11)$$

where $Y_r(q_u, \dot{q}_u)$ is a regression matrix and Φ_r is an unknown parameter vector containing the elements of K_{cu} and C_{cu} . The control force is:

$$f_c = Y_r \hat{\Phi}_r - D_f \dot{q}_c - K_f q_c \quad (3.12)$$

D_f and K_f are loosely referred to as the controller damping and stiffness coefficient matrices. As in section 3.3.2, it is convenient to treat the controller as an M-K-C system. $\hat{\Phi}_r$ is an adaptive set of parameter estimates governed by the adaptation law:

$$\dot{\hat{\Phi}}_r = -\Gamma_r \Upsilon^T P x_c \quad (3.13)$$

where $x_c = [q_c, \dot{q}_c]^T$, Γ_r is a symmetric and positive semidefinite matrix, and $\Upsilon^T = [[0], M_c^{-1} Y_r^T]$.

In order to guarantee stability, the following restrictions must be met:

- (A1) M_c is a symmetric and positive definite matrix ($M_c = M_c^T > 0$).
- (A2) $f_u(t) \in \mathcal{L}_\infty$ (the control force is bounded).
- (A3) The roots λ of $|\lambda^2 M_u + \lambda C_u + K_u| = 0$ have negative real parts.
- (A4) D_f and K_f are selected so that the roots λ of $|\lambda^2 M_c + \lambda(C_c + D_f) + (K_c + K_f)| = 0$ have negative real parts.

The proof of guaranteed stability involves forming a matrix A_c :

$$A_c = \begin{bmatrix} [0] & [I] \\ -M_c^{-1}(K_c + K_f) & -M_c^{-1}(D_c + D_f) \end{bmatrix} \quad (3.14)$$

which is the state space representation for the unforced controllable states accounting for the matrix gains D_f and K_f . If D_f and K_f are chosen so that condition (A4) above is met, then A_c is positive definite and all of the real parts of its eigenvalues are positive. This being the case, it can be shown that stability is guaranteed if there exists a positive definite matrix $P = P^T > 0$ (P is positive definite) such that the Lyapunov equation [5]:

$$A_c^T P + P A_c = -Q \quad (3.15)$$

can be solved for the matrix Q and $Q = Q^T > 0$, Q being a positive definite matrix.

In the case of the 5-DOF rocket model, only the payload and subcomponent are chosen to be controllable, thus:

$$q_c = \begin{bmatrix} X_P & X_1 \end{bmatrix}^T \quad q_u = \begin{bmatrix} X_L & X_U & X_I \end{bmatrix}^T$$

$$M_c = \begin{bmatrix} M_P & 0 \\ 0 & M_1 \end{bmatrix} \quad M_u = \begin{bmatrix} M_L & 0 & 0 \\ 0 & M_U & 0 \\ 0 & 0 & M_I \end{bmatrix}$$

$$K_c = \begin{bmatrix} (k_{IP} + k_{P1}) & -k_{P1} \\ -k_{P1} & k_{P1} \end{bmatrix} \quad K_u = \begin{bmatrix} k_{LU} & -k_{LU} & 0 \\ -k_{LU} & (k_{LU} + k_{UI}) & -k_{UI} \\ 0 & -k_{UI} & (k_{UI} + k_{IP}) \end{bmatrix}$$

$$C_c = \begin{bmatrix} (c_{IP} + c_{P1}) & -c_{P1} \\ -c_{P1} & c_{P1} \end{bmatrix} \quad C_u = \begin{bmatrix} c_{LU} & -c_{LU} & 0 \\ -c_{LU} & (c_{LU} + c_{UI}) & -c_{UI} \\ 0 & -c_{UI} & (c_{UI} + c_{IP}) \end{bmatrix}$$

$$K_{uc} = \begin{bmatrix} 0 & 0 \\ 0 & 0 \\ -k_{IP} & 0 \end{bmatrix} \quad K_{cu} = \begin{bmatrix} 0 & 0 & -k_{IP} \\ 0 & 0 & 0 \end{bmatrix}$$

$$C_{uc} = \begin{bmatrix} 0 & 0 \\ 0 & 0 \\ -c_{IP} & 0 \end{bmatrix} \quad C_{cu} = \begin{bmatrix} 0 & 0 & -c_{IP} \\ 0 & 0 & 0 \end{bmatrix}$$

$$\Phi_r = \begin{bmatrix} -k_{IP} \\ -c_{IP} \end{bmatrix} \quad \hat{\Phi}_r = \begin{bmatrix} -\hat{k}_{IP} \\ -\hat{c}_{IP} \end{bmatrix}$$

If only the states of the payload, and not the states of the subcomponent are measurable:

$$Y_r = \begin{bmatrix} X_I & \dot{X}_I \\ 0 & 0 \end{bmatrix} D_f = \begin{bmatrix} d_f & 0 \\ 0 & 0 \end{bmatrix} K_f = \begin{bmatrix} k_f & 0 \\ 0 & 0 \end{bmatrix} x_c = \begin{bmatrix} X_P \\ \dot{X}_P \end{bmatrix}$$

and the control law reduces to a negative feedback force on the payload:

$$f_p = -\hat{k}_{IP}X_I - \hat{c}_{IP}\dot{X}_I - k_fX_P - d_f\dot{X}_P \quad (3.16)$$

Equation 3.16 says that the first two terms involve \hat{k}_{IP} and \hat{c}_{IP} adapting to cancel out the vibration of the inert payload, while the second two terms involve k_f and d_f which are chosen to give the desired payload response.

To find the adaptation law, the following matrices are formed:

$$\Upsilon^T = \begin{bmatrix} 0 & \frac{X_I}{M_P} \\ 0 & \frac{\dot{X}_I}{M_P} \end{bmatrix} \quad P = \begin{bmatrix} p_{11} & p_{12} \\ p_{21} & p_{22} \end{bmatrix}$$

$$\dot{\hat{\Phi}}_r = \begin{bmatrix} -\dot{\hat{k}}_{IP} \\ -\dot{\hat{c}}_{IP} \end{bmatrix} \quad \Gamma_r = -M_P \text{ a scalar}$$

Where p_{ij} are the solutions to the Lyapunov equation, Equation 3.15. The adaptation law becomes:

$$\begin{aligned} \dot{\hat{k}}_{IP} &= X_I \left(p_{11} X_P + p_{12} \dot{X}_P \right) \\ \dot{\hat{c}}_{IP} &= \dot{X}_I \left(p_{21} X_P + p_{22} \dot{X}_P \right) \end{aligned} \quad (3.17)$$

For the Simulink™ model, the following values are chosen:

$$d_f = 2\pi (2 \cdot \zeta_c \cdot \omega_1) \quad k_f = M_P \cdot (2\pi \cdot \omega_1)^2$$

$$Q = \begin{bmatrix} q_1 & 0 \\ 0 & q_2 \end{bmatrix}$$

Where:

$$\zeta_c = (\text{the controller damping}) = \frac{\sqrt{2}}{2}$$

$$q_1 = (k_{IP} + k_{P1} + k_f) - 1 - \frac{k_{P1}}{M_1}$$

$$q_2 = -\frac{k_{P1}}{M_P} + \frac{k_{P1}}{m_1} - 1$$

which result in a positive definite P with the controller damping and k_f as chosen above. Also, the adaptive controller uses the same proportional feedback gain as the PID controller and the skyhook damper:

$$K_p = 5 \cdot 10^{-10}$$

These values are then coded into the Simulink™ model as shown in Figure 3.8 .

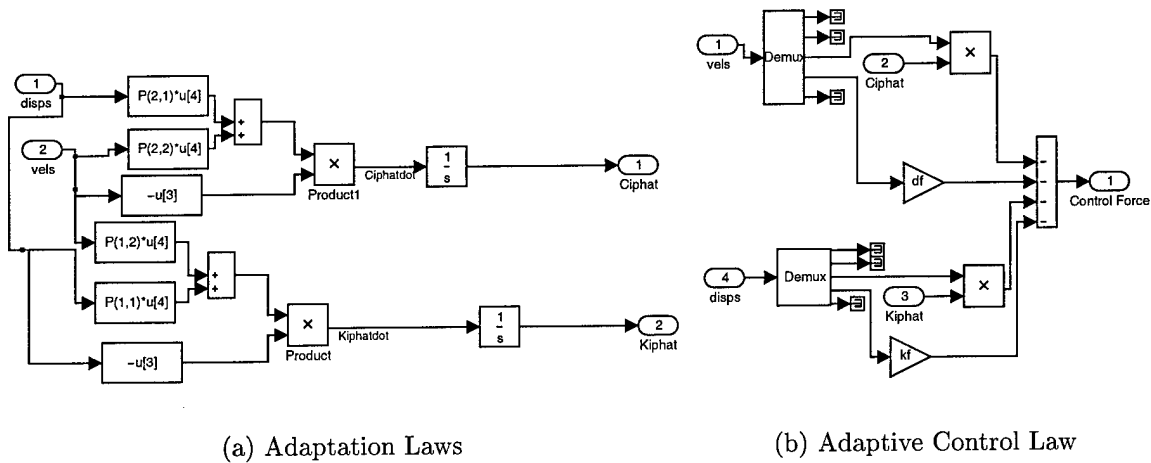


Figure 3.8 Simulink Model Adaptation Laws and Adaptive Control Laws

The vibration isolation methods range from simple passive isolation to the complex adaptive vibration isolator. The passive isolator only allows for a fixed stiffness and damping value between the inert component and payload. The PID controller and skyhook damper feed back certain payload states through a fixed gain control law. The adaptive isolator measures multiple component states and adapts its control law gains to cancel vibrations input to the payload, while also using fixed gains to give the payload a desired response. Chapter IV explores the effects of these different isolation methodologies.

IV. Data Description and Analysis

This chapter presents the data collected from multiple runs of the 5 DOF rocket model using the control methodologies described in Chapter III. In Section 4.1, the model is run for the entire flight profile from liftoff to just after fourth stage burnout. To investigate vibration isolation, the model is run for two main cases: a fixed resonant burn frequency at 50 Hz (Section 4.2) and a swept resonant burn frequency ramping from 45 to 60 Hz during the first stage burn (Section 4.3). Within these two sections, passive, active and adaptive vibration isolation results are compared. In the case of investigating the different isolation schemes, only the first 90 seconds of flight are presented which include liftoff, the first stage engine cutoff and second stage engine firing.

4.1 Full Run

Figure 4.1 shows the profile of the entire launch vehicle flight from liftoff to payload separation. For this mission profile, the full run ($t = 0$ sec to $t = 710$ sec) Simulink™ model produces the payload acceleration profile shown in Figure 4.2. Each stage cutoff, separation, coast, and next stage firing are evident in Figure 4.2 as large acceleration changes. The full run results show the acceleration of the center of gravity and the noise accelerations on the payload. The following sections, analyzing the performance of the different isolation schemes, separate the center of gravity accelerations from the noise accelerations and only take into account the first 90 seconds of the mission profile.

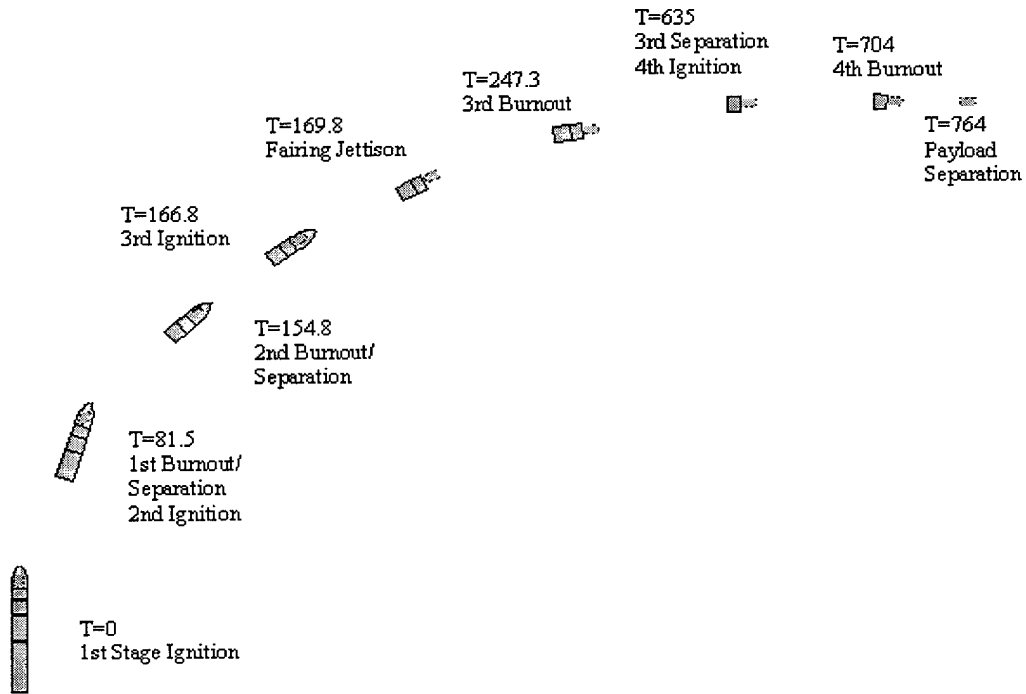


Figure 4.1 Launch Vehicle Mission Profile

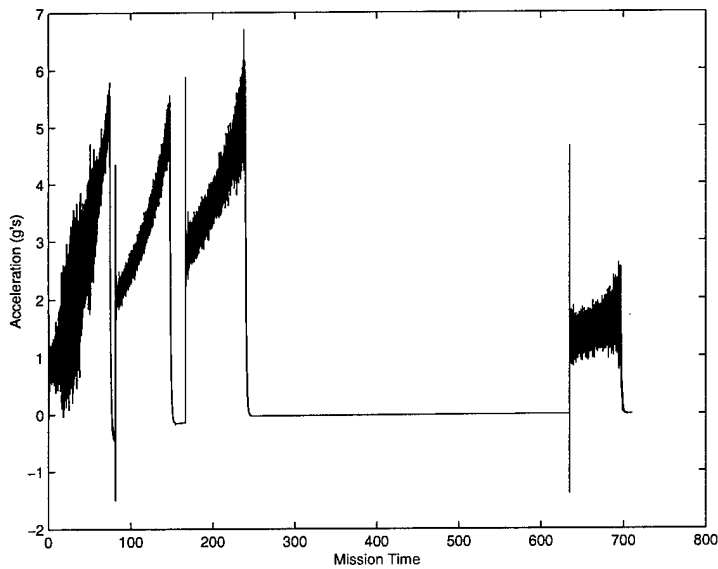


Figure 4.2 Full Run Payload Acceleration Profile

4.2 *Fixed Resonant Burn Frequency*

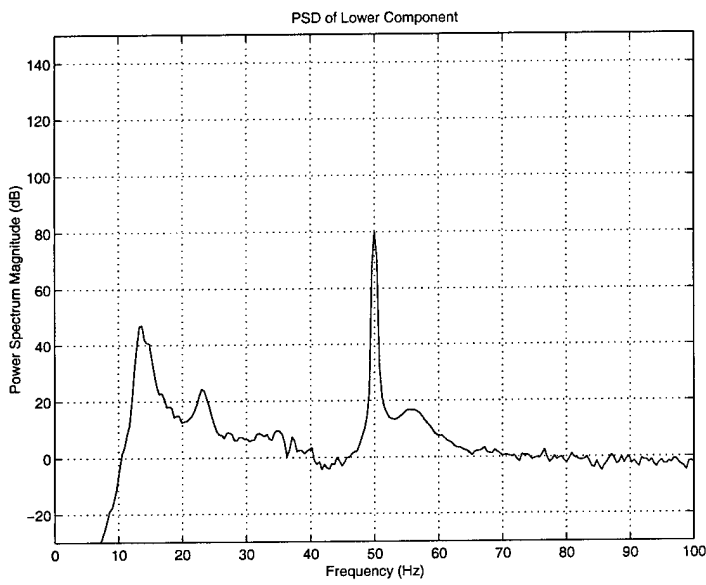
4.2.1 *Baseline Results.* For the baseline case, the model simulated a payload "hardmounted" to the inert stage during the first 90 seconds of flight. The resonant burn frequency is set at 50 Hz. The payload resonant frequency was set at 200 Hz to act as a stiff spring with low damping ($\zeta = 0.01$). The acceleration Power Spectral Densities (PSDs) of the lower, upper and inert components are shown in Figure 4.3.

The PSDs show the dynamic energy of each component over a range of frequencies. For a discussion on PSDs, root-mean-square (RMS) and modal analysis, reference Inman [12]. Notice the clearly defined modes near 12Hz, 22 Hz, and 50Hz.

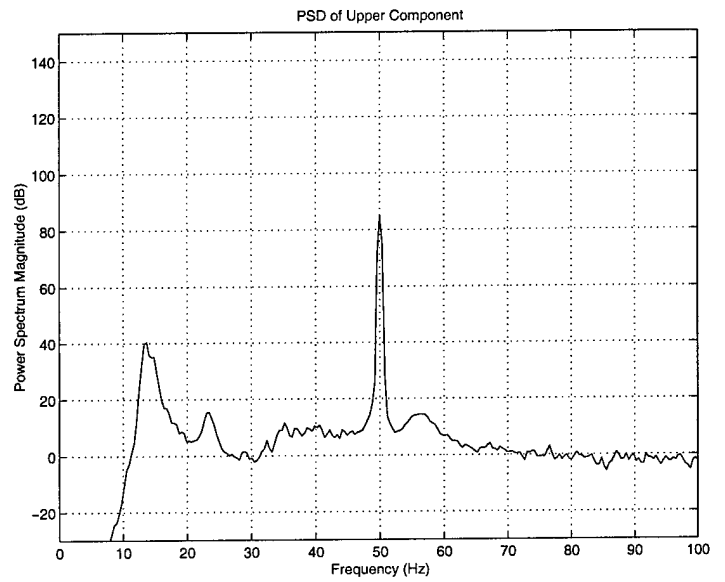
The 12 Hz peak is due to the first launch vehicle mode. The 22 Hz peak is due to the second launch vehicle mode. The 50 Hz peak is due to a combination of the resonant burn frequency and the fact that the subcomponent is tuned to 50 Hz. The subcomponent is tuned to 50 Hz to present a worse-case scenario for the subcomponent being excited by a resonant burn of the same frequency.

The modes of the rocket are shown plainly in the PSDs, however, since the rocket's mass is changing over time, the modes actually move in frequency over the first 90 seconds of flight. Figure 4.4 shows the spectrograms for the lower, upper, and inert components for the baseline case.

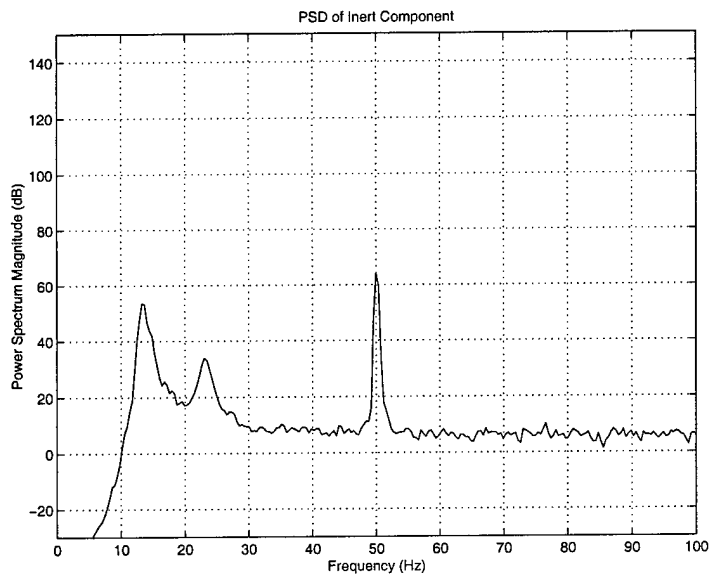
Darker areas on the spectrograms represent a higher magnitude response. The spectrograms show that the fixed resonant burn frequency remains at 50Hz, while the first and second launch vehicle modes increase in frequency until the first stage separation (represented by a broad-band shock). The frequency increase is due to expending propellant and reducing the mass of the lower and upper components. The inert component shows no second launch vehicle mode.



(a) Lower Component Acceleration PSD

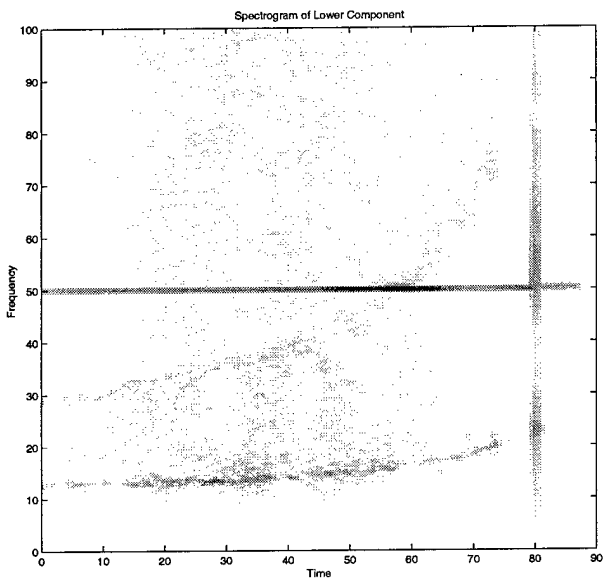


(b) Upper Component Acceleration PSD

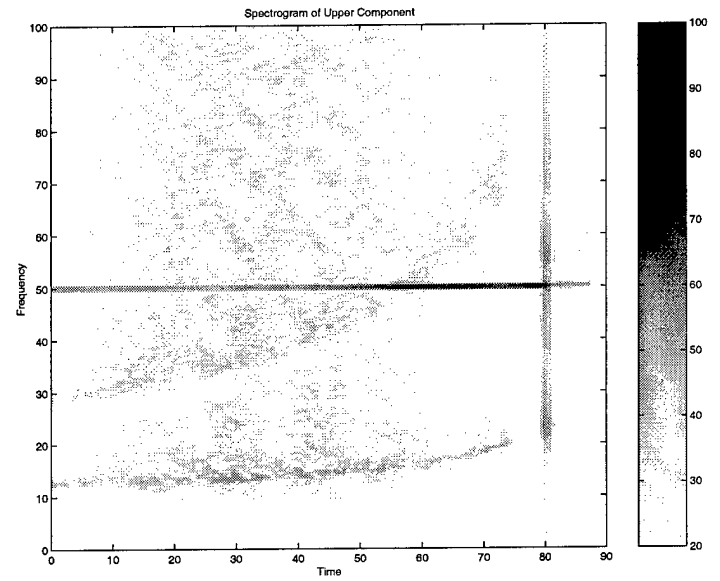


(c) Inert Component Acceleration PSD

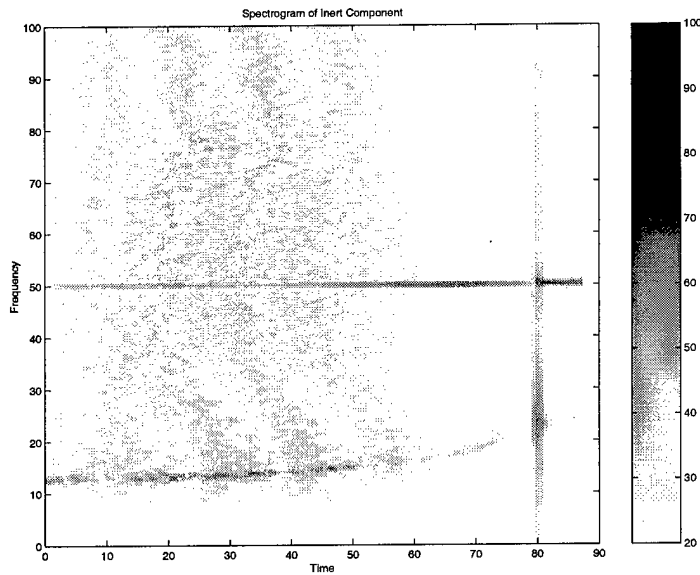
Figure 4.3 Lower, Upper, and Inert Component Acceleration PSDs, Baseline Case



(a) Lower Component Acceleration Spectrogram



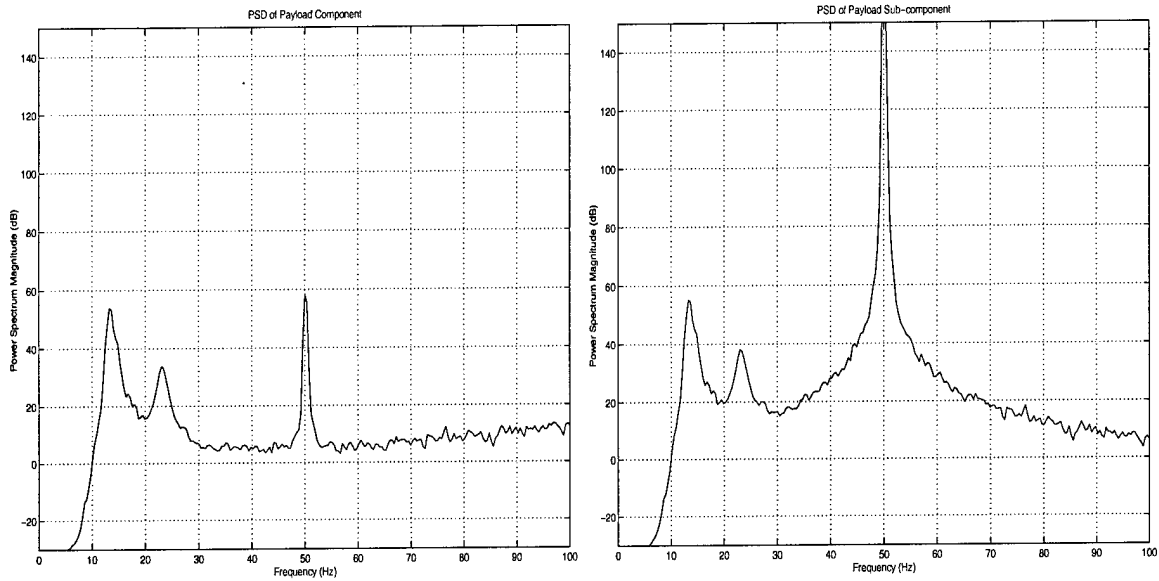
(b) Upper Component Acceleration Spectrogram



(c) Inert Component Acceleration Spectrogram

Figure 4.4 Lower, Upper, and Inert Component Acceleration Spectrograms, Base-line Case

Of particular interest are the responses of the payload and the 50 kg subcomponent. Their PSDs are shown in Figure 4.5, and their spectrograms are shown in Figure 4.6. Notice the high frequency noise amplification beyond the 50 Hz payload



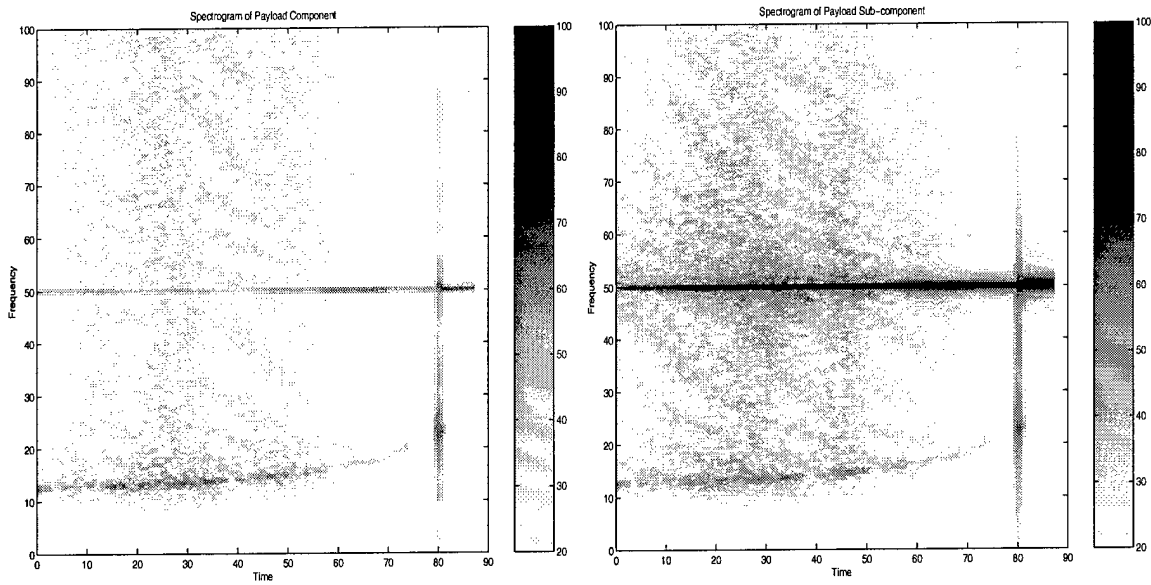
(a) Payload Acceleration PSD

(b) Subcomponent Acceleration PSD

Figure 4.5 Payload and Subcomponent Acceleration PSDs, Baseline Case

mode. This necessitates some form of payload isolation. Since the subcomponent is tuned to 50 Hz, it's response at that frequency is greatly magnified by the 50 Hz resonant burn frequency. The subcomponent was tuned to 50 Hz with light damping ($\zeta = 0.01$) between it and the payload. The subcomponent's PSD does not show high frequency noise amplification because tuning it to 50 Hz, in effect, creates a passive isolator between the payload and the subcomponent. Compared with the spectrogram of the payload, the spectrogram of the subcomponent shows clear intensification of the 50 Hz resonant burn mode.

Since the subcomponent acceleration spectrogram in Figure 4.6 shows such a significant 50 Hz mode intensification, varying its mass or natural frequency may



(a) Payload Acceleration Spectrogram

(b) Subcomponent Acceleration Spectrogram

Figure 4.6 Payload and Subcomponent Acceleration Spectrograms, Baseline Case

dramatically change the behavior of the payload. Figure 4.7 shows the effect of varying the subcomponent mass. In this case, the natural frequency of the subcomponent remained at 50 Hz, while the mass percentage of the payload made up of the subcomponent varied from one percent to fifty percent as the total payload mass remained at 1780 kg. There is very little effect in varying the subcomponent mass until the subcomponent makes up a full fifty percent of the payload. At this point, a higher frequency mode near 110 Hz affects the payload in addition to the subcomponent 50 Hz mode.

Varying the subcomponent natural frequency also shows little change in the payload response. Figure 4.8 shows the results of this effect in the payload PSD. For this case, the subcomponent natural frequency (ω_1) varied from 10 Hz to 300 Hz while the mass of the subcomponent remained at 50 kg and the mass of the payload remained at 1780 kg.

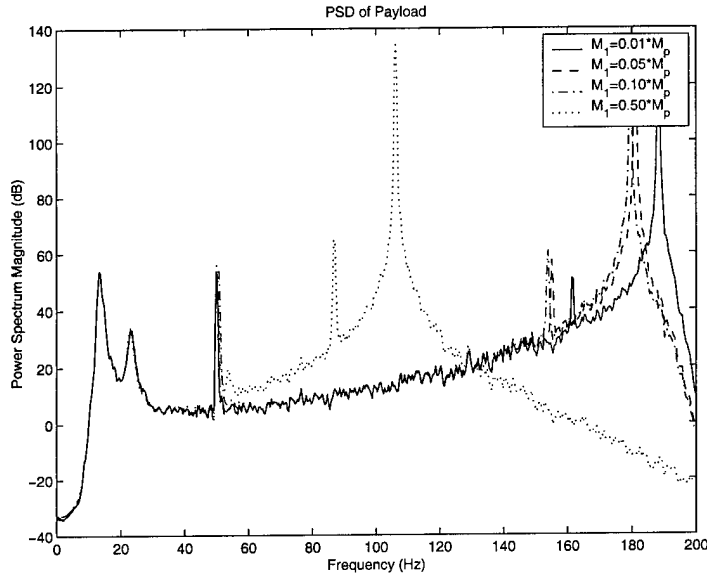


Figure 4.7 Payload Effects of Varying Subcomponent Mass

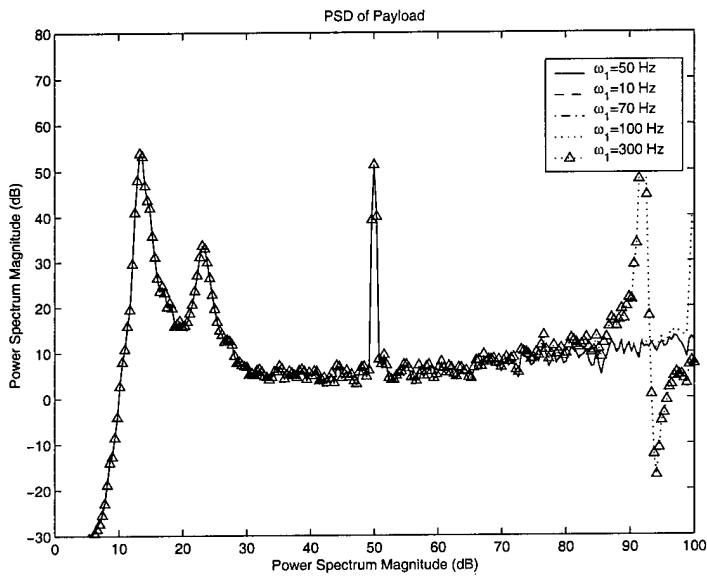


Figure 4.8 Payload Effects of Varying Subcomponent Frequency

Looking at Figures 4.9 and 4.10, varying subcomponent mass has very little effect on the subcomponent response until the subcomponent comprises fifty percent of the mass of the payload. Varying the subcomponent natural frequency has little effect on the first two launch vehicle modes. Those two modes remain largely unchanged except for the case when $\omega_1 = 10$ Hz. At this low subcomponent natural

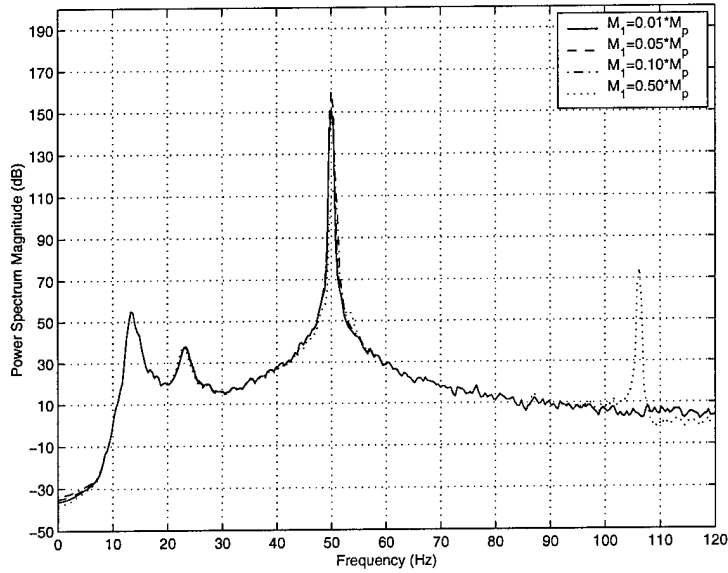


Figure 4.9 Subcomponent Effects of Varying Subcomponent Frequency

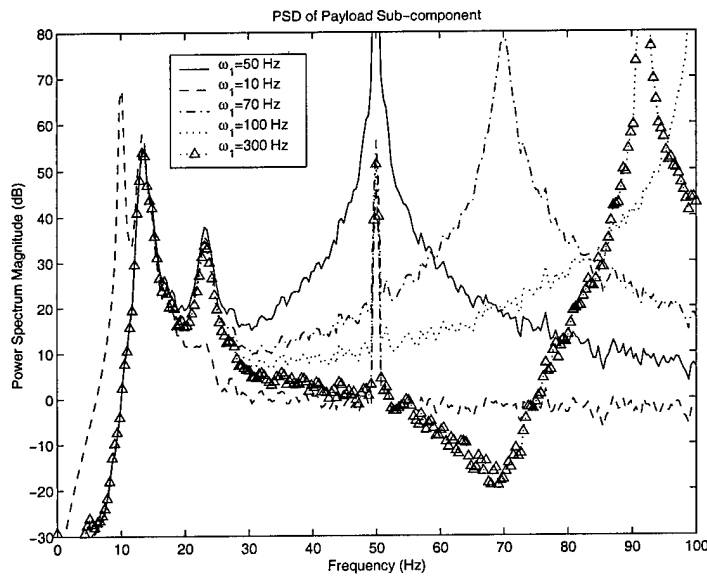


Figure 4.10 Subcomponent Effects of Varying Subcomponent Frequency

frequency, a clear 10 Hz mode shows up in the subcomponent PSD, taking away energy from the second launch vehicle mode near 22 Hz.

In contrast, the changing subcomponent frequency has a significant effect on the 50 Hz resonant burn mode. This mode is greatly intensified when the subcom-

ponent natural frequency matches it at 50 Hz. However, this mode contains much less energy at different subcomponent natural frequencies.

4.2.2 Passive Control Results. Adding a passive isolator between the inert component and the payload is desired to eliminate high frequency noise amplification as presented in Section 1.1. Figure 4.11 below shows the acceleration PSD of the payload with a 27 Hz passive isolator. Beyond approximately 60

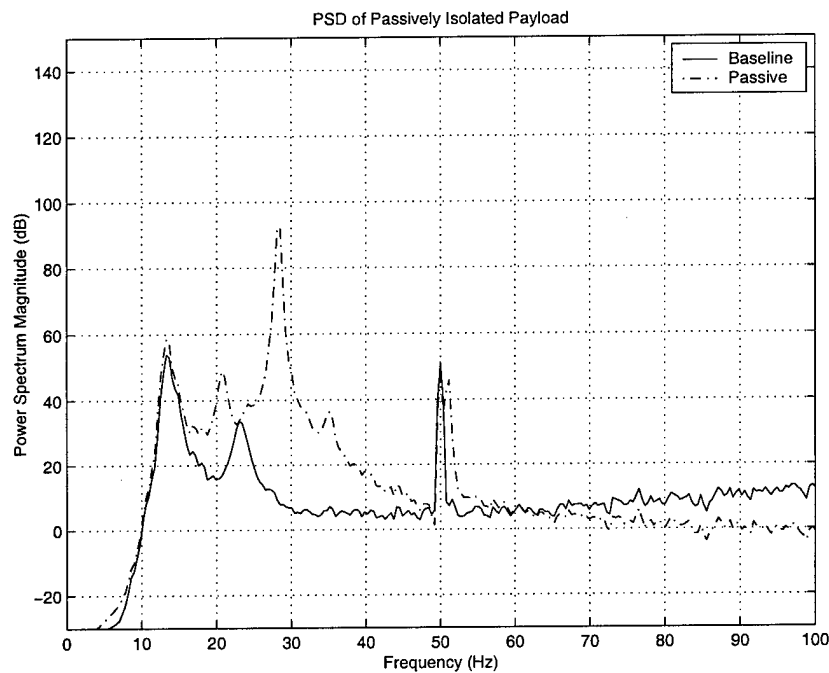


Figure 4.11 Payload PSD, 27Hz Isolator

Hz, the vibration of the payload is effectively isolated, however the 27 Hz isolator added a dominant 27 Hz mode to the payload response and added energy to the 12 Hz and 22 Hz modes. The spectrogram of the payload (Figure 4.12) also shows this addition of the 27 Hz mode. A darker band than in the baseline case show how the amplification of the 10 Hz mode persists over time.

The PSD of the subcomponent (Figure 4.13) shows a decrease in the energy at the 50 Hz mode and effective high frequency noise isolation. However, the sub-

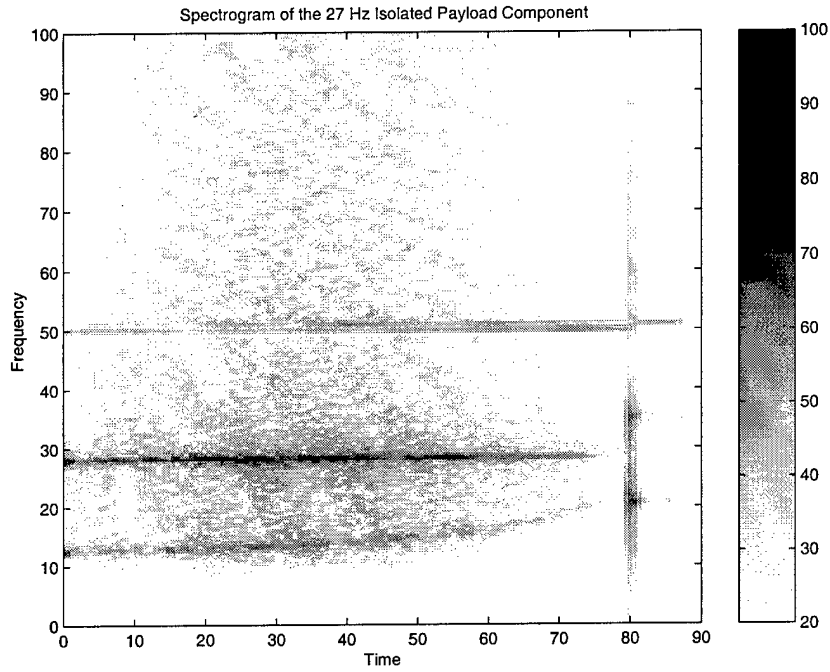


Figure 4.12 Payload Spectrogram, 27Hz Isolator

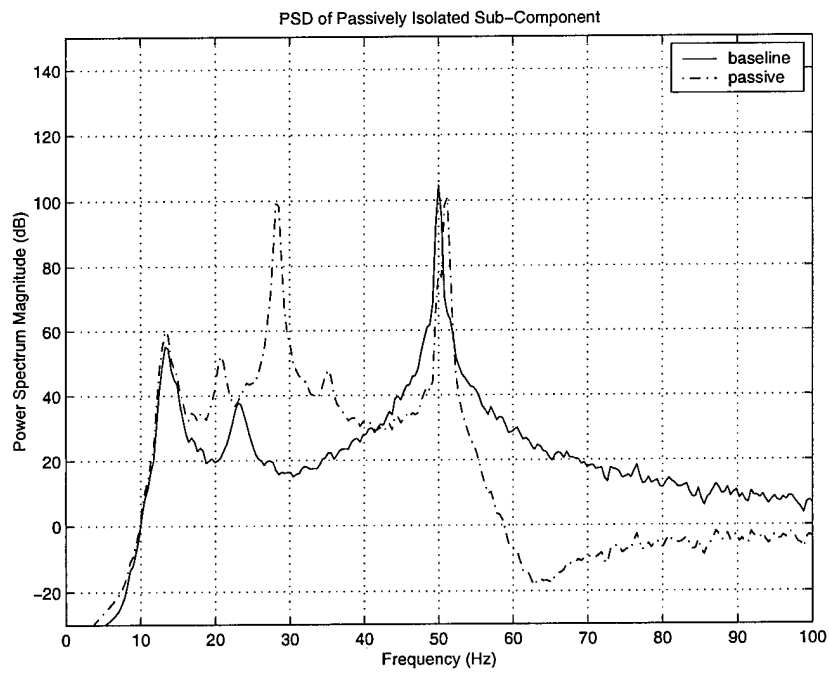


Figure 4.13 Subcomponent PSD, 27Hz Isolator

component's interaction with the payload cause the 27 Hz mode and the lower mode amplification to appear in the subcomponent.

The spectrogram of the subcomponent's response due to a 27 Hz payload isolator (Figure 4.14) appears lighter along the 50 Hz mode and in the higher frequency

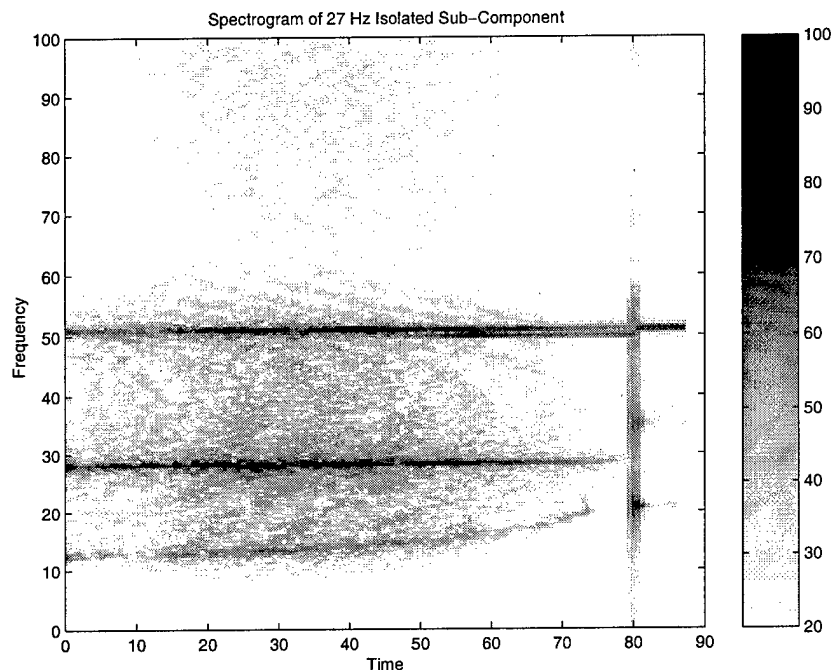


Figure 4.14 Subcomponent Spectrogram, 27Hz Isolator

realm when compared to the baseline case.

Different isolator frequencies obtain different isolation results. Figure 4.15 shows the maximum acceleration in g's of the passively isolated payload and subcomponent. The 25 Hz low isolator frequency was chosen due to the possibility of interfering with launch vehicle guidance and control instrumentation with low bandwidths [14]. The upper 40 Hz isolator frequency limit was chosen to avoid amplification of the 50 Hz resonant burn frequency and the natural response of the 50 Hz-tuned subcomponent. Figure 4.15 shows a dramatic reduction in the maximum g environment of the payload when compared to the baseline case for the full range of isolator frequencies. However, as the isolator frequency approaches the 50 Hz

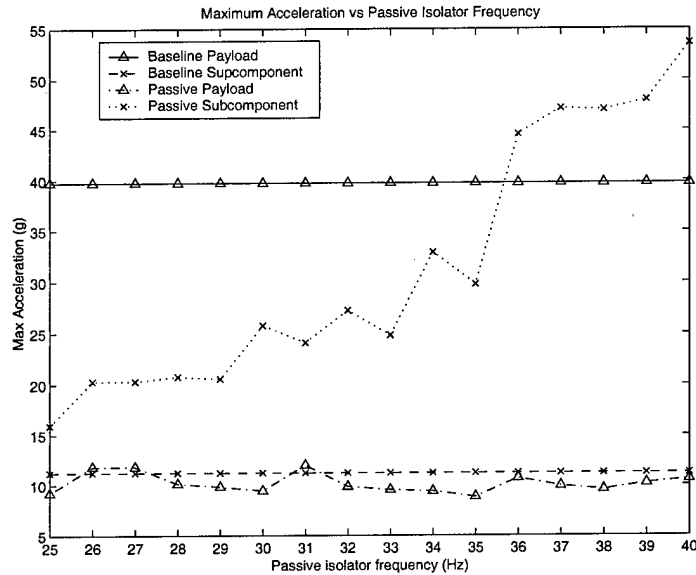


Figure 4.15 Maximum Acceleration vs. Isolator Frequencies: Fixed Resonant Burn

subcomponent resonant frequency, the subcomponent experiences higher maximum acceleration. In fact, the subcomponent's maximum acceleration is worse across all isolator frequencies than the baseline hard-mounted payload case. This subcomponent effect does not affect the payload, however, which remains in a relatively low level maximum g environment.

Figure 4.16 shows the root-mean-square (RMS) acceleration of the passively isolated payload and subcomponent. As was the case for the maximum acceleration environment, the RMS accelerations of the payload are dramatically decreased, while the subcomponent's g environment is worse than the baseline case. Again, the subcomponent encounters higher g loading as the isolator frequency approaches its 50 Hz natural frequency.

4.2.3 Active Control Results. Section 4.2.2 showed a degradation in subcomponent loads as the isolator natural frequency approaches the natural frequency of the subcomponent. This same effect takes place in the active control results, however it is evident in the loads on the payload. Figure 4.17 shows a payload

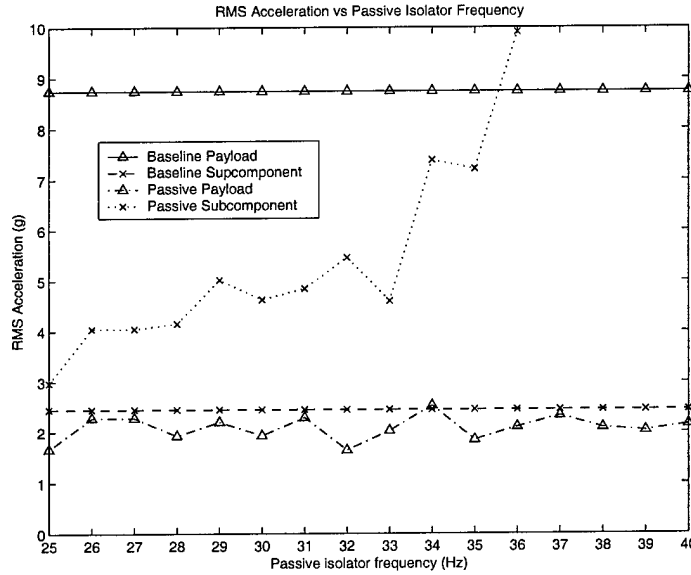
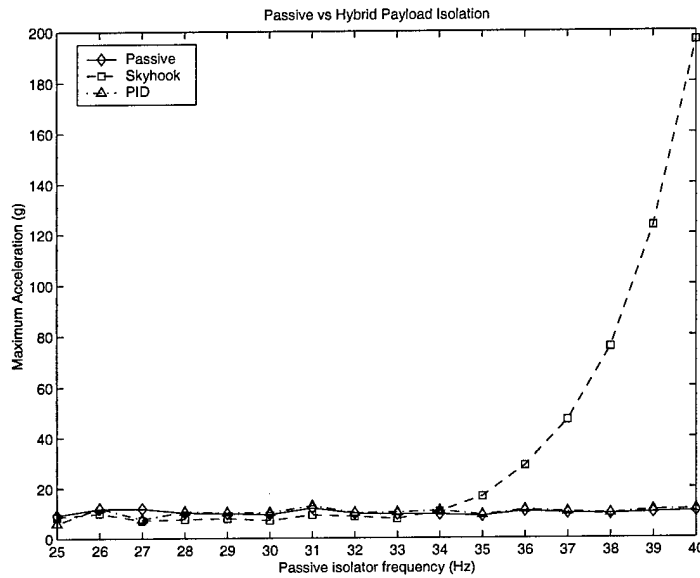


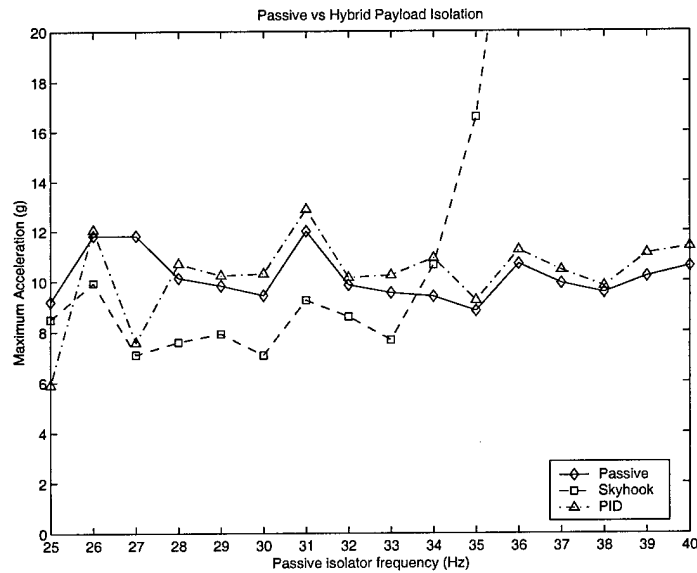
Figure 4.16 RMS Acceleration vs. Isolator Frequencies: Fixed Resonant Burn

maximum acceleration comparison of passive isolation, PID control, and skyhook damping control. This shows that the skyhook damper achieves the best maximum acceleration results when compared to passive and PID vibration isolation until an isolator frequency of about 34 Hz. For the skyhook damper, the subcomponent interacts with the response of the payload, especially when the passive isolator frequency is near ω_1 . On the other hand, the PID controller allows for very little interaction of the passive isolator frequency and the subcomponent natural frequency.

Figure 4.18 shows the RMS acceleration of the active control and the passive isolation. Again, the skyhook damper shows the best results until, approximately, a 34 Hz passive isolator frequency. The skyhook damper theory is a structural construct, while the PID theory is not. The skyhook damper's response to the subcomponent resonance may be a result of its structural construct.

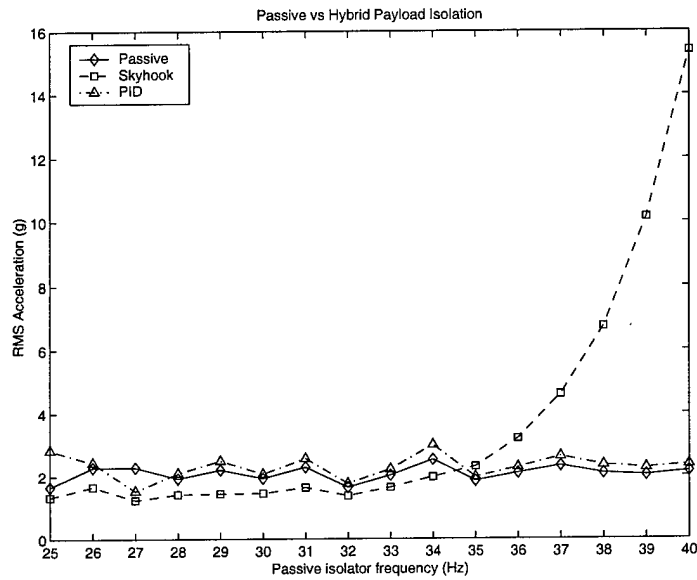


(a) Maximum Accelerations

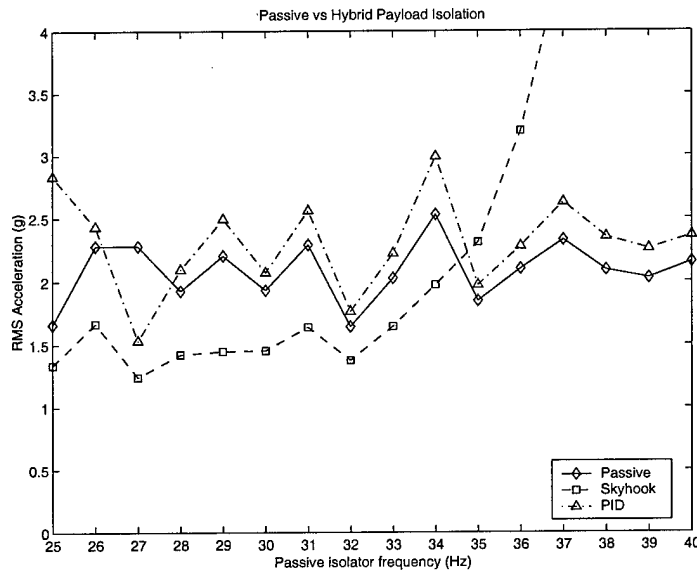


(b) Zoom

Figure 4.17 Active Control: Maximum Payload Acceleration vs. Isolator Frequencies, Fixed Resonant Burn



(a) RMS Accelerations

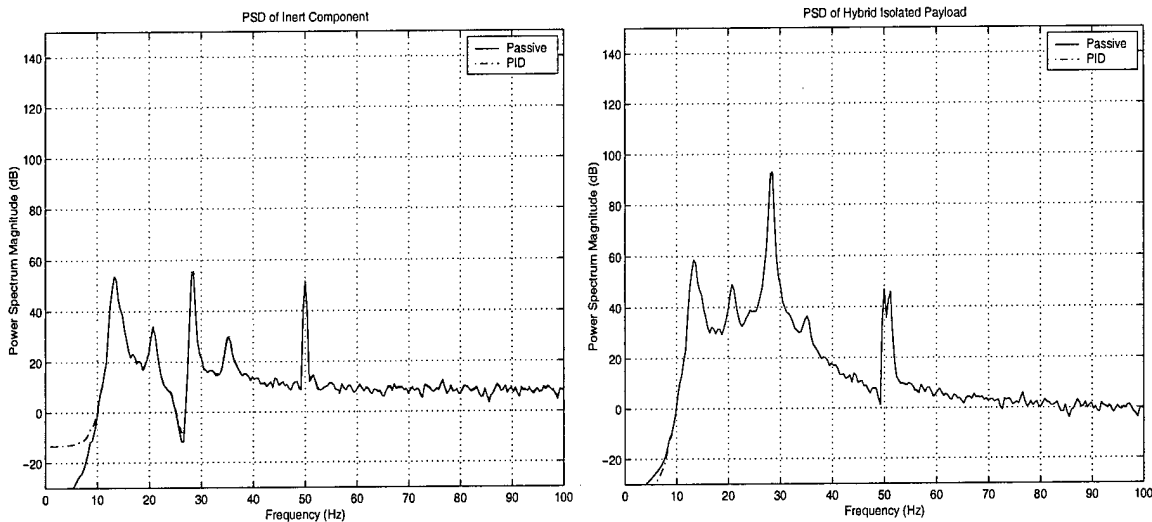


(b) Zoom

Figure 4.18 Active Control: RMS Payload Acceleration vs. Isolator Frequencies, Fixed Resonant Burn

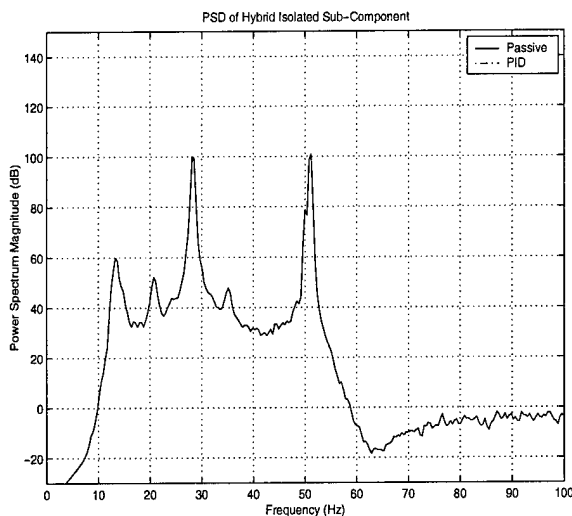
4.2.3.1 PID Control.

PID control showed no degradation due to the changing isolator natural frequencies. Figure 4.19 shows the effects of PID control with a 27 Hz passive isolator on the different modes of the launch vehicle.



(a) Inert Component Acceleration PSD

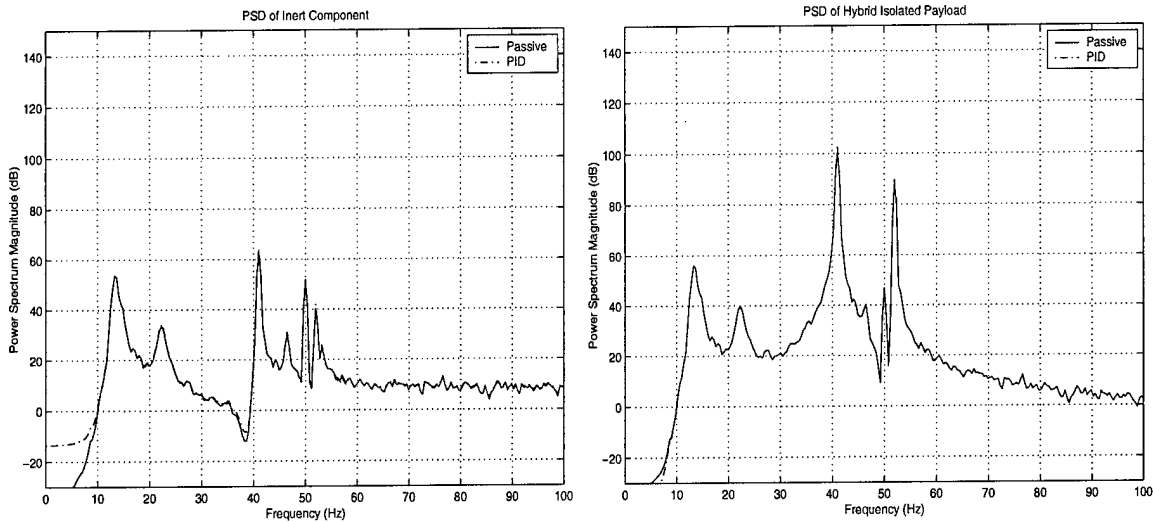
(b) Payload Acceleration PSD



(c) Subcomponent Acceleration PSD

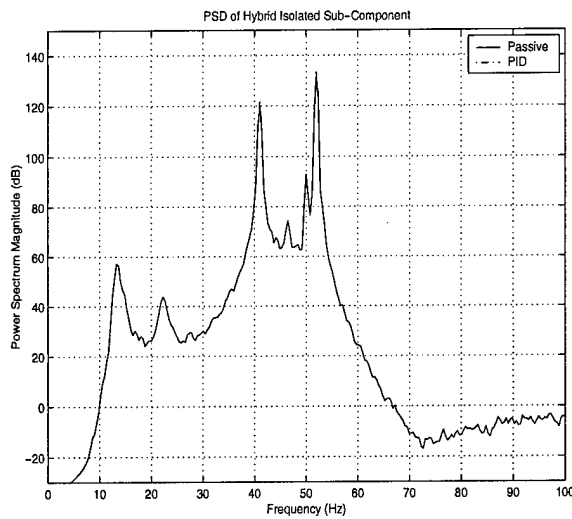
Figure 4.19 PID Controller, 27 Hz Passive Isolator Inert Component, Payload, and Subcomponent Acceleration PSDs: Fixed Resonant Burn

The PID controller also showed no degradation at passive isolator frequencies near the subcomponent natural frequency. Figure 4.20 shows that there is little degradation when the passive isolator frequency is at 40 Hz. Although working



(a) Inert Component Acceleration PSD

(b) Payload Acceleration PSD



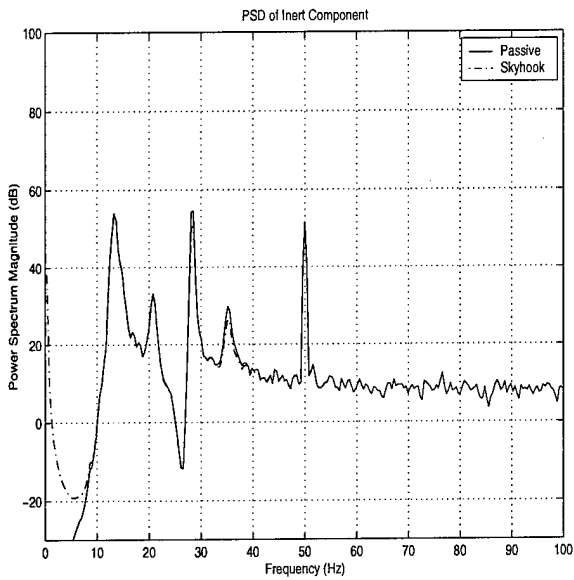
(c) Subcomponent Acceleration PSD

Figure 4.20 PID Controller, 40 Hz Passive Isolator Inert Component, Payload, and Subcomponent Acceleration PSDs: Fixed Resonant Burn

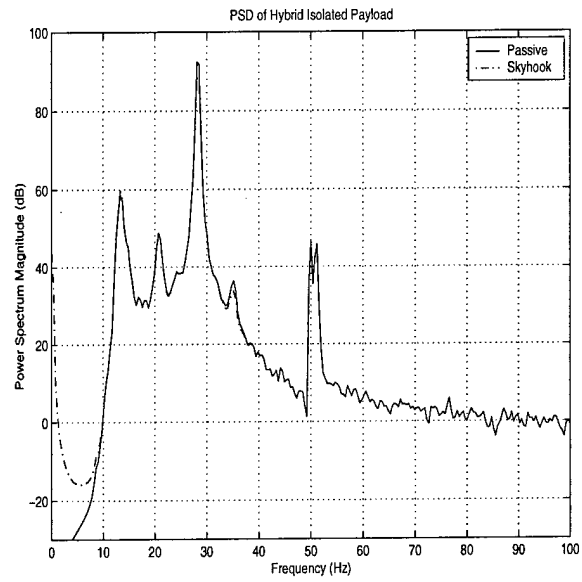
effectively to reduce the maximum and RMS accelerations over all frequencies, the PID controller shows very little modal control.

4.2.3.2 Skyhook Damper. The skyhook damper showed good maximum and RMS acceleration results for isolator frequencies lower than 34 Hz. The PSD's of the Inert component, payload, and subcomponent for a 27 Hz passive isolator with the skyhook damper are in Figure 4.21. Notice there is little attenuation or degradation for each of the PSDs in Figure 4.21. The degradation comes at higher isolator frequencies as shown in the PSDs in Figure 4.22. Shown in the 40 Hz passive isolator PSDs, the performance of the skyhook damper is badly degraded for both the payload and subcomponent at this isolator frequency. However, the PSD of the Inert component is relatively unchanged from the purely passive isolator case.

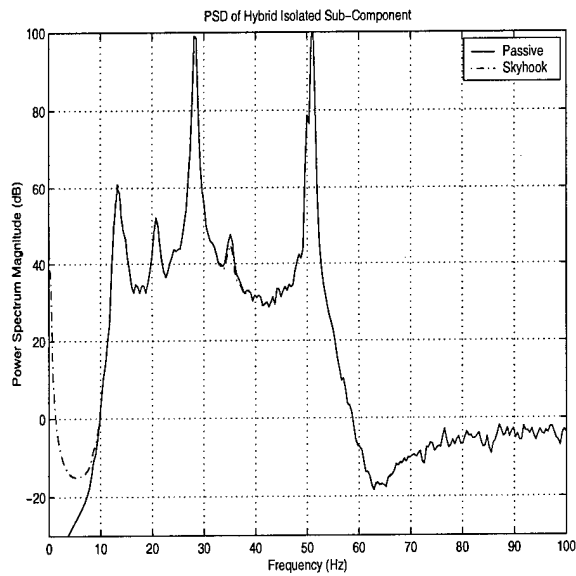
The skyhook damper was designed to attenuate the isolator mode. This section showed very little attenuation of the isolator mode. Section 3.3.2 discussed choosing the controller damping ratio. In this case, the controller damping ratio could not be chosen high enough to attenuate the passive isolator mode without driving the rest of the launch vehicle unstable.



(a) Inert Component Acceleration PSD

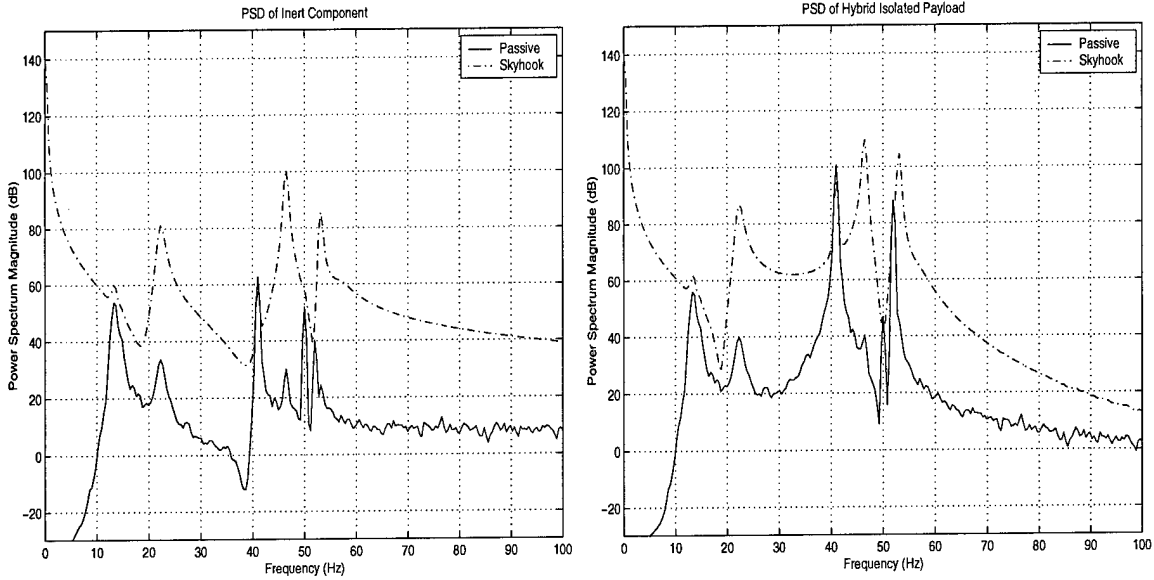


(b) Payload Acceleration PSD



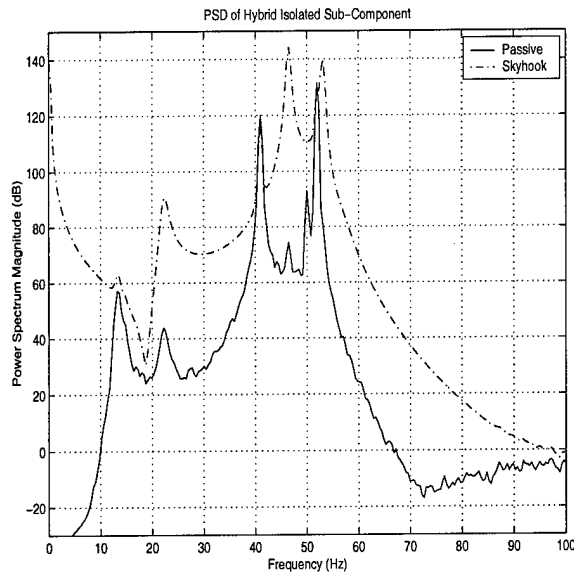
(c) Subcomponent Acceleration PSD

Figure 4.21 Skyhook Damper, 27 Hz Passive Isolator Inert Component, Payload, and Subcomponent Acceleration PSDs: Fixed Resonant Burn



(a) Inert Component Acceleration PSD

(b) Payload Acceleration PSD

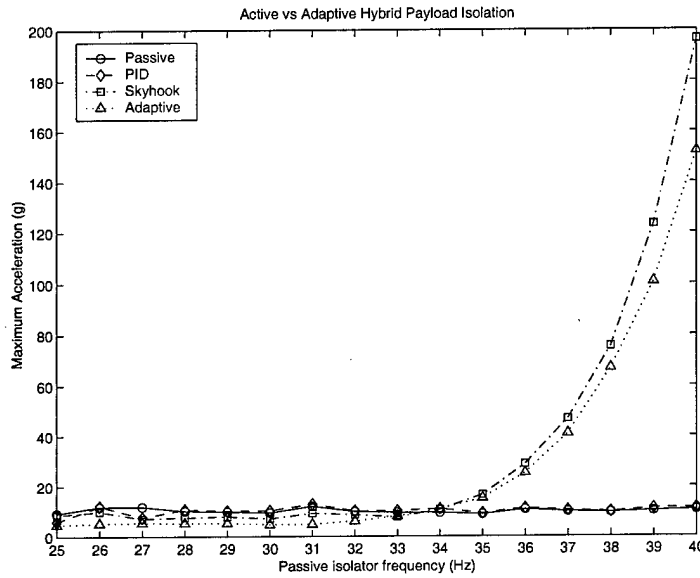


(c) Subcomponent Acceleration PSD

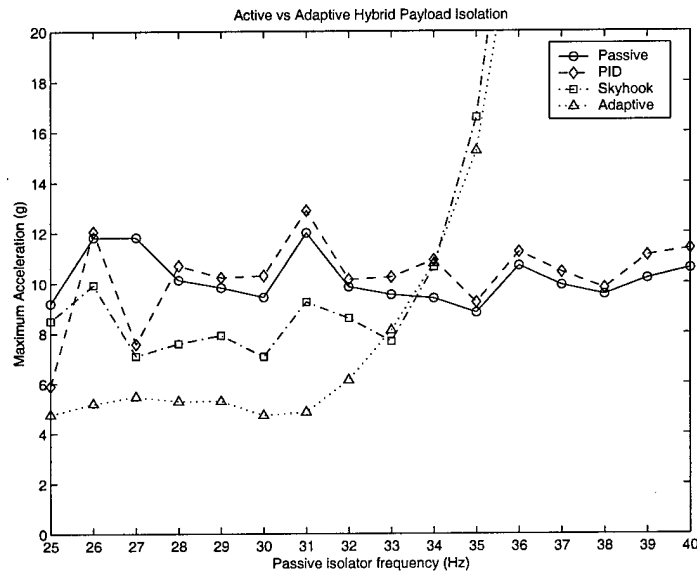
Figure 4.22 Skyhook Damper, 40 Hz Passive Isolator Inert Component, Payload, and Subcomponent Acceleration PSDs: Fixed Resonant Burn

4.2.4 Adaptive Control Results. Figure 4.23 shows the maximum accelerations for the adaptively controlled payload over a range of isolator frequencies. Comparable to the results in Figure 4.17, Figure 4.23 shows that the adaptive controller exhibits the same behavior as the skyhook damper. The adaptive controller effectively cancels out the vibrations of the inert component on the payload. However, at higher isolator frequencies, the force of the inert component vibrations are transmitted through the payload to the subcomponent. The subcomponent continues to vibrate, and, at isolator frequencies of approximately 34 Hz and higher, takes over as the dominant force on the payload.

Figure 4.24 shows the RMS accelerations experienced by the payload with adaptive control. The adaptive isolation RMS values suggest that using the adaptive vibration isolation scheme can significantly reduce the RMS acceleration experienced by the payload at lower isolator frequencies. Also when compared to the RMS payload results for the active isolators (Figure 4.18, Section 4.2.3), the isolator frequency at which the adaptive controller is significantly degraded is pushed out to 38 Hz vs. 34 Hz with the skyhook damper. In both maximum and RMS payload accelerations, the adaptive controller shows significant load reduction at lower passive isolator frequencies when compared to the passive only isolator and the two active hybrid isolators.

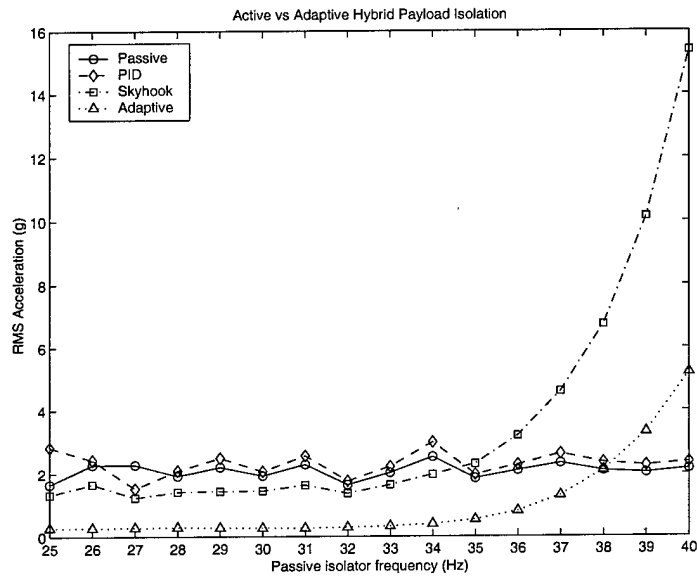


(a) Maximum Accelerations

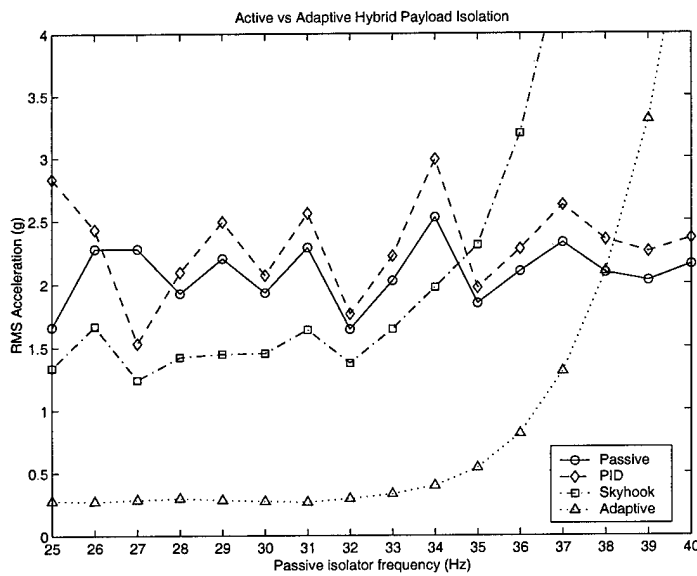


(b) Zoom

Figure 4.23 Adaptive Control: Maximum Payload Acceleration vs. Isolator Frequencies, Fixed Resonant Burn



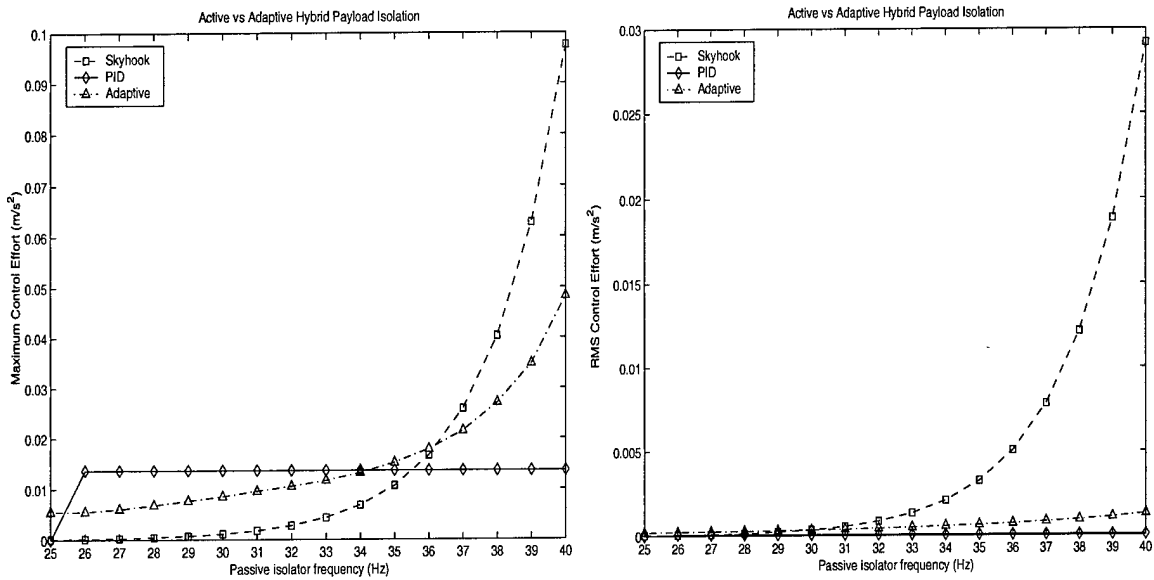
(a) RMS Accelerations



(b) Zoom

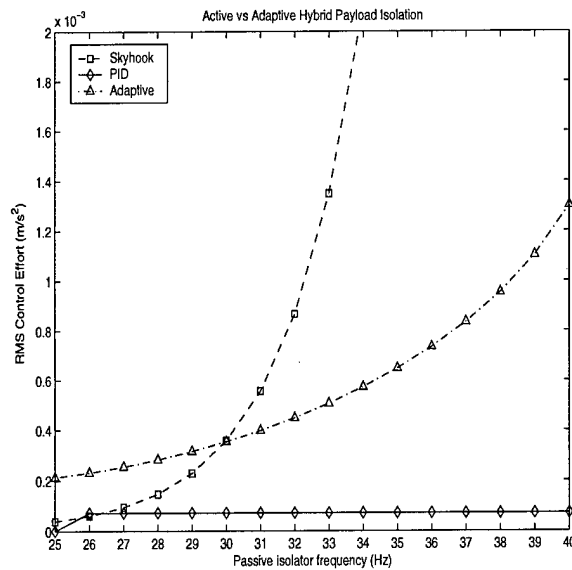
Figure 4.24 Adaptive Control: RMS Payload Acceleration vs. Isolator Frequencies, Fixed Resonant Burn

Figure 4.25 shows the maximum and RMS control effort needed to produce the results for the fixed resonant burn frequency with hybrid isolators. The PID



(a) Maximum Control Effort

(b) RMS Control Effort



(c) RMS Control Effort (zoom)

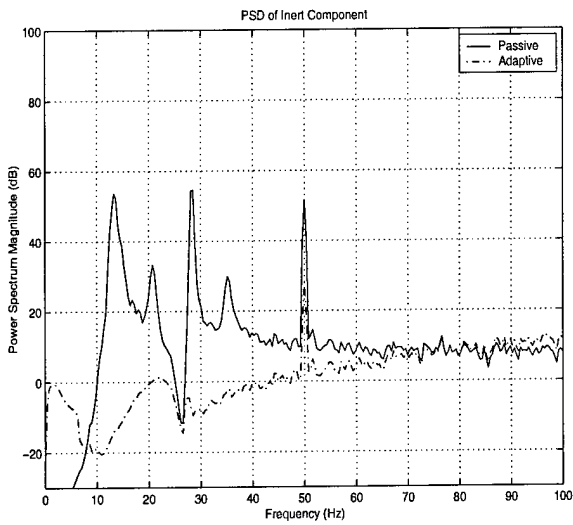
Figure 4.25 Hybrid Control Effort: Fixed Resonant Burn

controller seemed to require the least amount of control effort across the range of passive isolator frequencies.

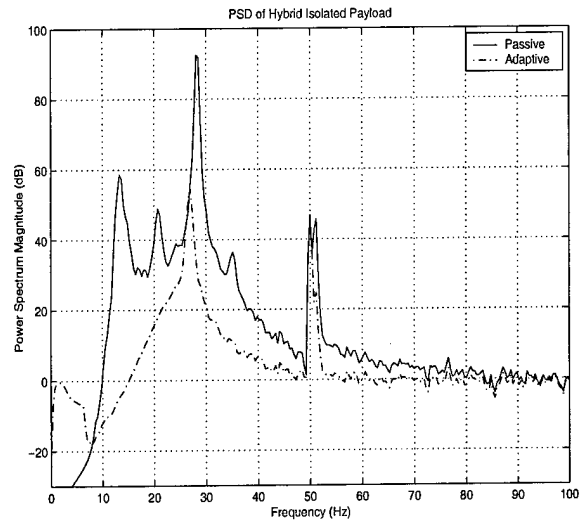
The skyhook damper and adaptive controller trade off the amount of control effort required at lower passive isolator frequencies. As the passive isolator frequency approaches the 50 Hz subcomponent natural frequency and resonant burn frequency, the skyhook damper and adaptive controller begin to require drastically more control effort.

The adaptive control PSDs show the significant improvement in isolation over the passively isolated case (see Figure 4.26). For all three rocket components, the 12 Hz and 22 Hz launch vehicle modes were effectively eliminated. The fixed gain portions (k_f and d_f) of the adaptive controller were designed to improve the response around the 50 Hz mode. These fixed gains did not result in significant reduction of the response exactly at 50 Hz (similar to the skyhook damper), but did dramatically reduce the response at frequencies near the 50 Hz mode. The 27 Hz isolator mode is also significantly reduced.

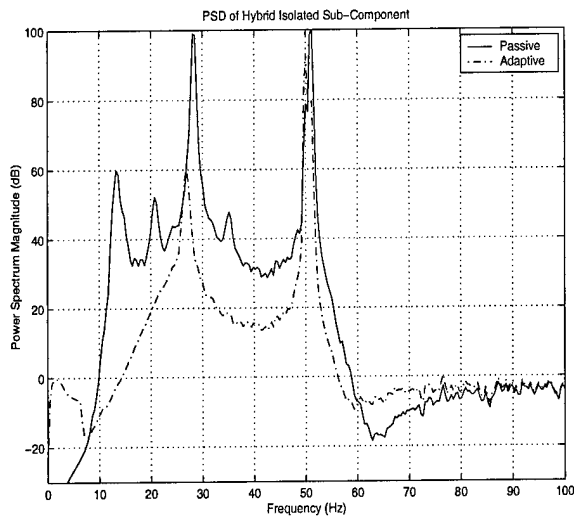
Note that the PSD of the inert component in Figure 4.26 is almost completely flat. The adaptive controller may have adapted to completely remove the modal content of the inert component's vibration to keep the payload from vibrating. However, the subcomponent continues to exhibit a strong 50 Hz response.



(a) Inert Component Acceleration PSD



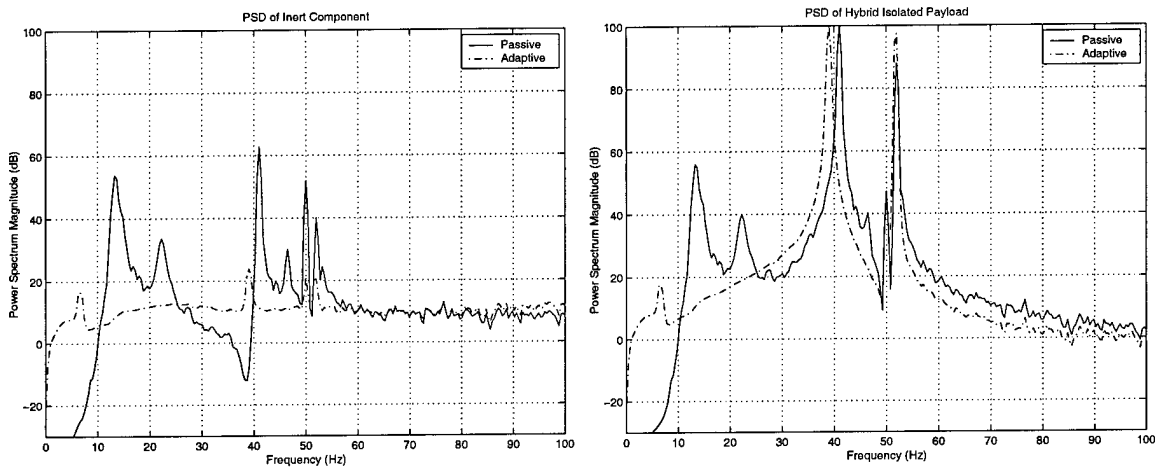
(b) Payload Acceleration PSD



(c) Subcomponent Acceleration PSD

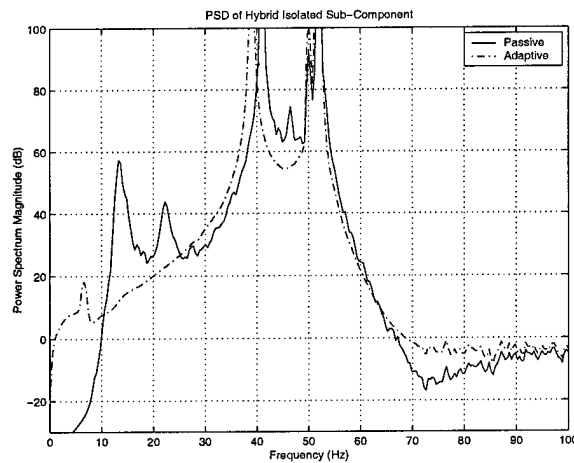
Figure 4.26 Adaptive Control, 27 Hz Passive Isolator Inert Component, Payload, and Subcomponent Acceleration PSDs: Fixed Resonant Burn

As noted in Figures 4.23 and 4.24, the adaptive controller exhibited degraded response for isolator frequencies over 38 Hz. Figure 4.27 shows the PSDs for the adaptive controller with a 40 Hz isolator. The first two low frequency launch vehicle modes are again eliminated for all components, but the 40 Hz isolator mode and the 50 Hz subcomponent and resonant burn mode is badly degraded. Again, the PSD of the inert component is almost completely flat.



(a) Inert Component Acceleration PSD

(b) Payload Acceleration PSD



(c) Subcomponent Acceleration PSD

Figure 4.27 Adaptive Control, 40 Hz Passive Isolator Inert Component, Payload, and Subcomponent Acceleration PSDs: Fixed Resonant Burn

4.3 Ramp Resonant Burn Frequency

The results in Section 4.2 showed a 50 Hz mode due to both the resonant burn frequency and the subcomponent natural frequency. This section separates the resonant burn frequency from the vibration of the subcomponent by ramping the resonant burn from 45 Hz to 60 Hz. The effect is apparent in a sample PSD in Figure 4.28. The energy in the 50 Hz mode is now distributed over a range of frequencies. Evident in the spectrograms of the ramp resonant burn (Figure 4.29)

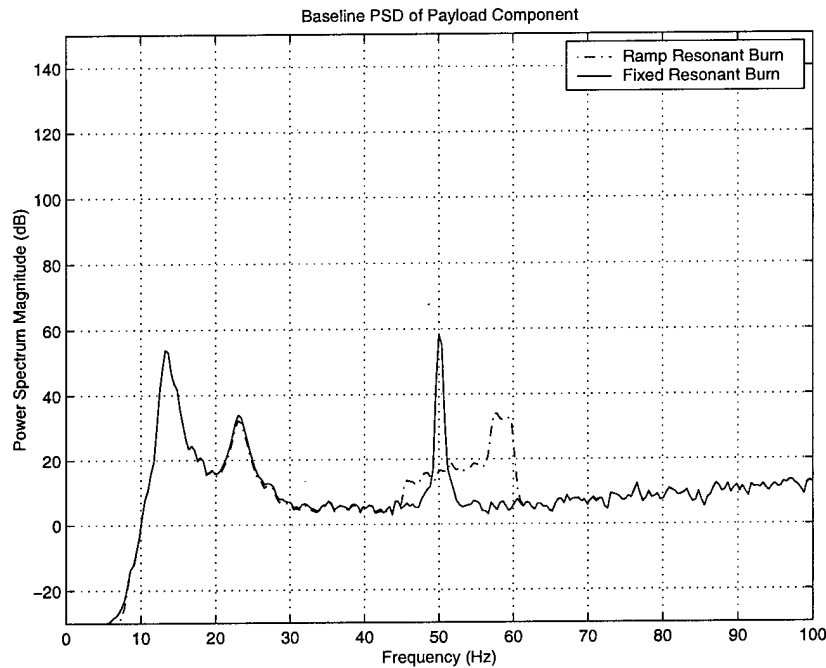
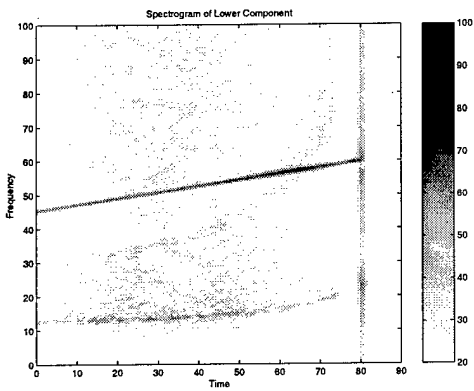
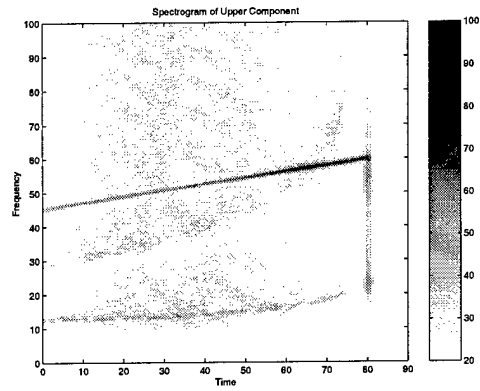


Figure 4.28 Sample PSD: Ramp vs Fixed Resonant Burn

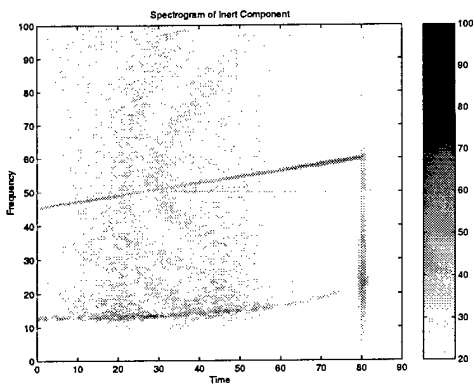
is the linearly time varying resonant burn from 45 Hz to 60 Hz during the first stage of flight. Except for in the subcomponent, the resonant burn is the major feature in each component of the rocket. For the subcomponent, its 50 Hz natural frequency is the dominant feature. In the following sections, it is this subcomponent natural frequency that drives the response of the payload as well, once the payload is effectively isolated from the vibrations of the lower, upper, and inert components.



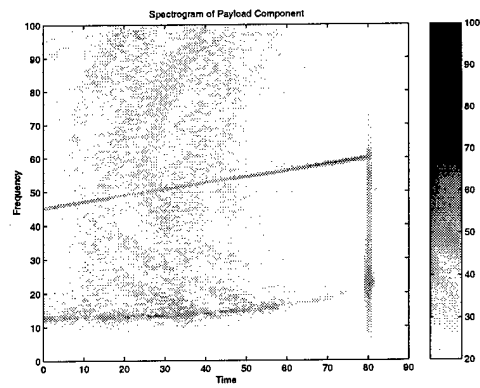
(a) Lower Component Acceleration Spectrogram



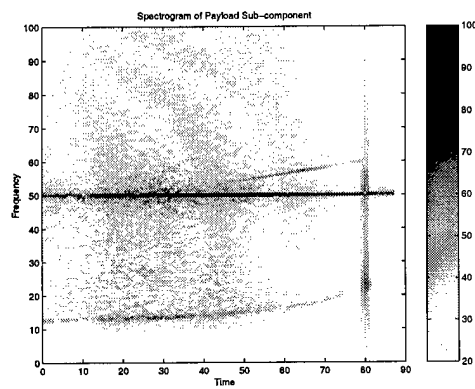
(b) Upper Component Acceleration Spectrogram



(c) Inert Component Acceleration Spectrogram



(d) Payload Acceleration Spectrogram



(e) Subcomponent Acceleration Spectrogram

Figure 4.29 Acceleration Spectrograms, Ramp Resonant Burn

4.3.1 Baseline Results.

Figure 4.30 shows the PSDs for the baseline case with a ramp resonant burn sweeping from 45 Hz to 60 Hz during the first 90 seconds of flight. The PSDs in Figure 4.30 are for the lower four components only. For these four components, the energy in the 50 Hz mode that existed for

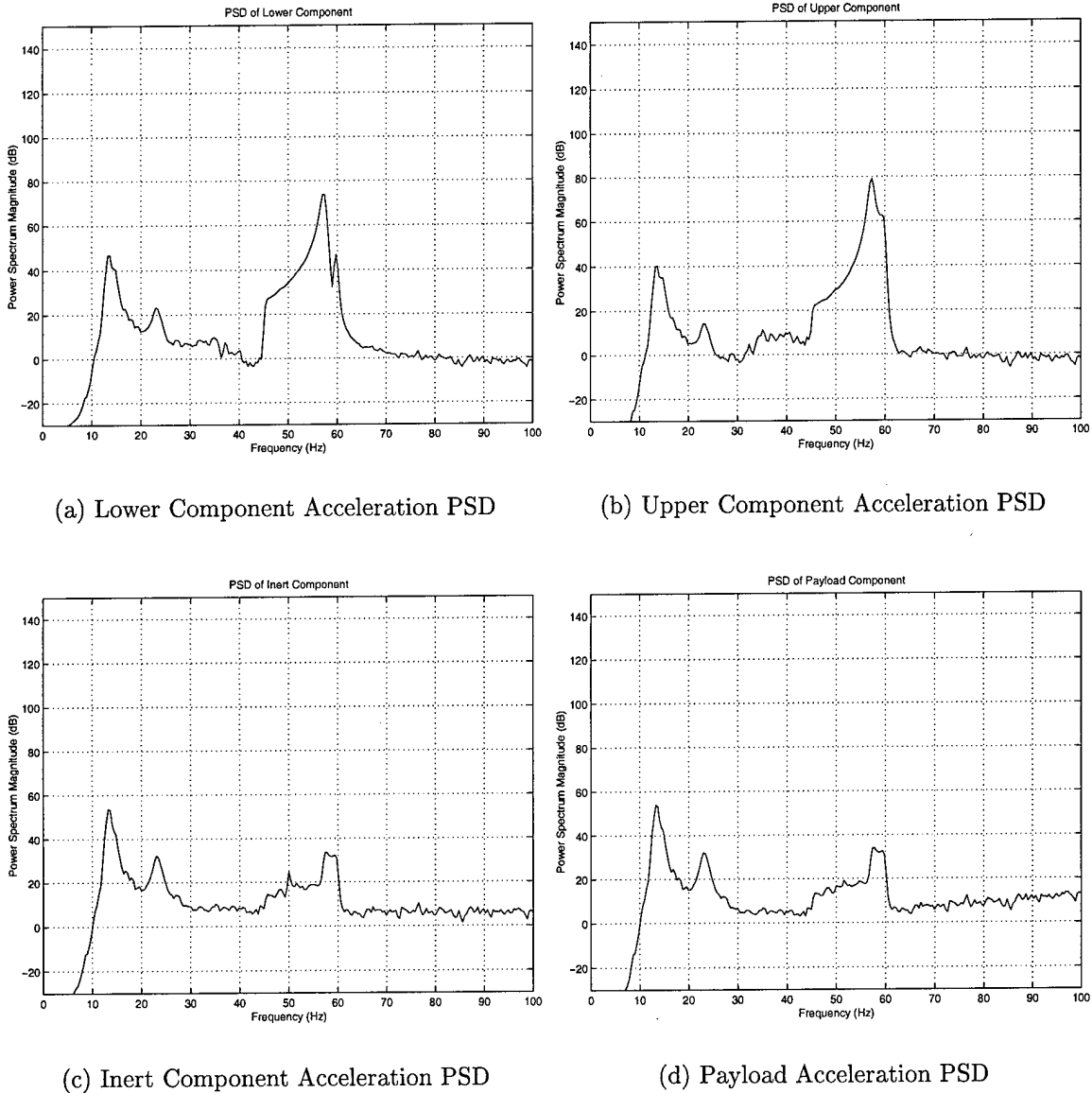


Figure 4.30 Lower Four Component Acceleration PSDs, Baseline Case: Ramp Resonant Burn

the fixed resonant burn frequency case, is now spread over the 45-60 Hz range. The

lower and upper components are more affected by the resonant burn than the inert component and payload.

With the ramp resonant burn, only the subcomponent experiences a significant 50 Hz mode, as shown in Figure 4.31. The subcomponent 50Hz mode is primarily a result of its natural frequency rather than of the resonant burn. However, when compared to the response in the fixed resonant burn frequency case (Figure 4.5), there is some reduction in the subcomponent's 50 Hz mode, since the resonant frequency is not purely at 50 Hz.

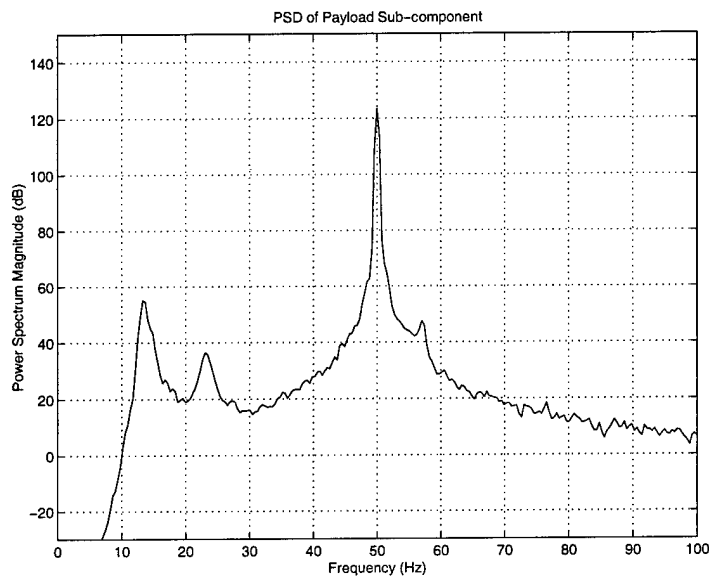
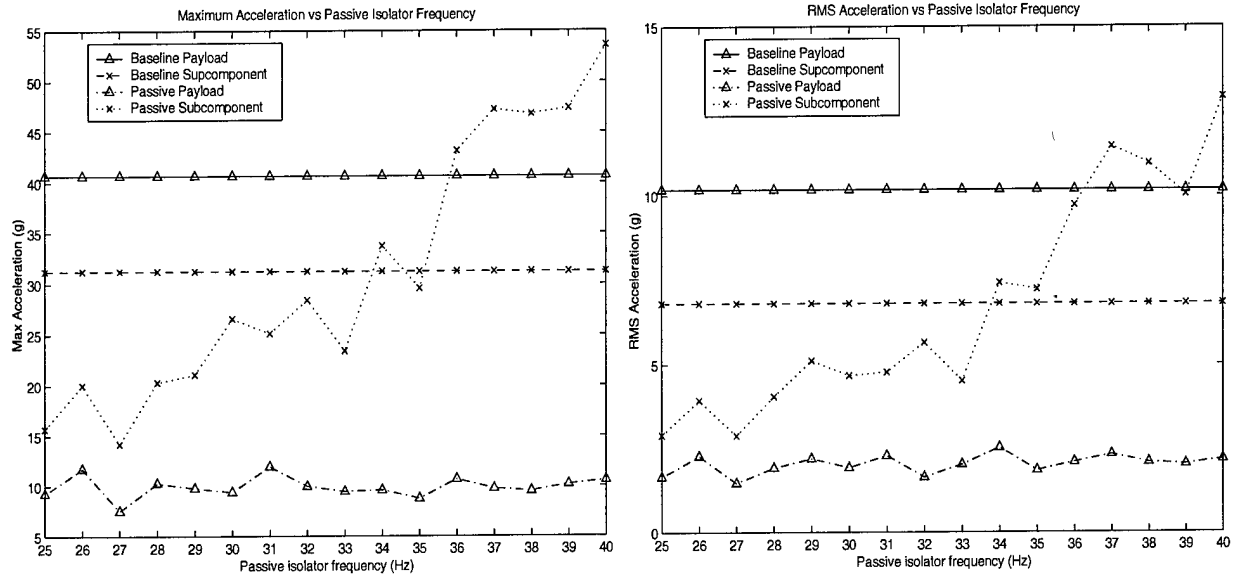


Figure 4.31 Subcomponent Acceleration PSD, Baseline Case: Ramp Resonant Burn

4.3.2 Passive Control Results. As discussed in Section 4.2.2,

different isolator frequencies result in different maximum and RMS accelerations.

Figure 4.32 shows these results. The best passive isolation results for the payload



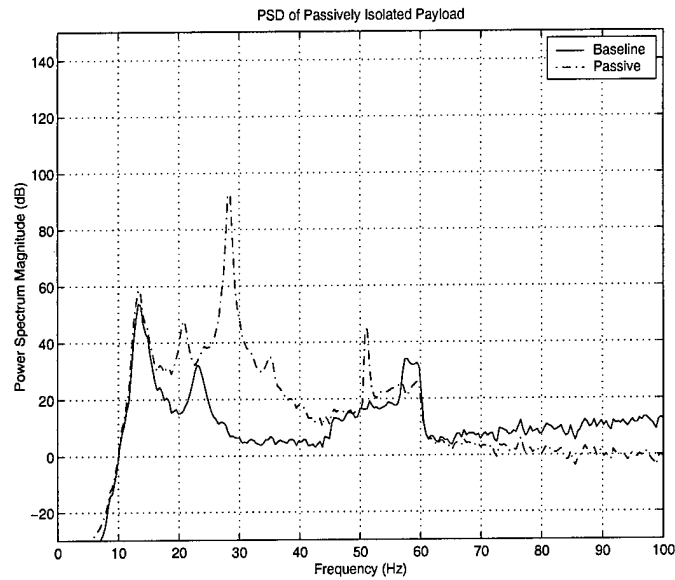
(a) Maximum Accelerations vs. Isolator Frequencies: Ramp Resonant Burn

(b) RMS Accelerations vs. Isolator Frequencies: Ramp Resonant Burn

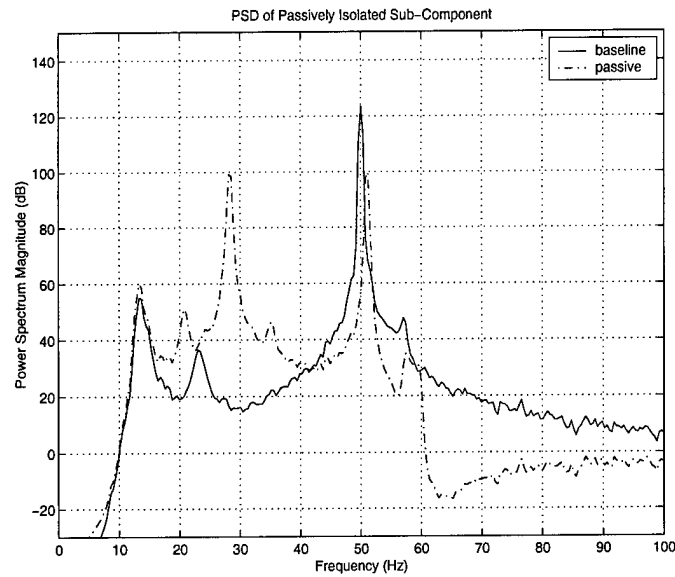
Figure 4.32 Maximum and RMS Accelerations: Ramp Resonant Burn

occur when the passive isolator frequency is at 27 Hz. For the subcomponent, as the passive isolator frequency approaches the 50 Hz subcomponent resonant frequency, the maximum and RMS accelerations begin to increase unfavorably.

Figure 4.33 shows the PSDs for the passive ramp resonant burn case. The passive isolator again shows good high frequency attenuation. Notice in the payload PSD that the passive isolator has isolated the payload, however the payload now shows a 50 Hz mode. Since the payload is isolated from the inert component, this 50 Hz mode is coming from the subcomponent vibration.



(a) Payload Acceleration PSD

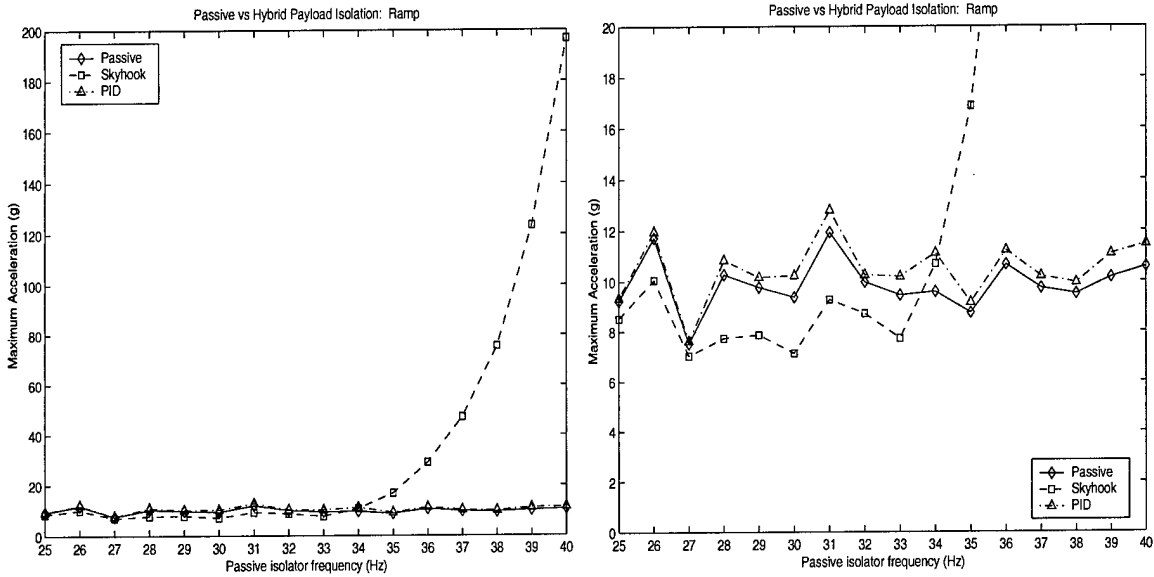


(b) Subcomponent Acceleration PSD

Figure 4.33 Passive Isolation: 27 Hz Passive Isolator Payload and Subcomponent Acceleration PSDs: Fixed Resonant Burn

4.3.3 Active Control Results.

Figure 4.34 shows similar results to Figure 4.17 in Section 4.2.3, but for the 45-60 Hz ramp resonant burn. Again, the maximum accelerations are all between 6 and 20 g's, except for with



(a) Maximum Accelerations

(b) Maximum Accelerations (zoom)

Figure 4.34 Active Control: Maximum Acceleration vs. Isolator Frequencies, Ramp Resonant Burn

the skyhook damper, where the payload undergoes increased maximum g loading at isolator frequencies higher than 34 Hz.

Figure 4.35 shows the actively isolated RMS accelerations for the ramp resonant burn case. As was the case for the fixed resonant burn frequency, the skyhook damper

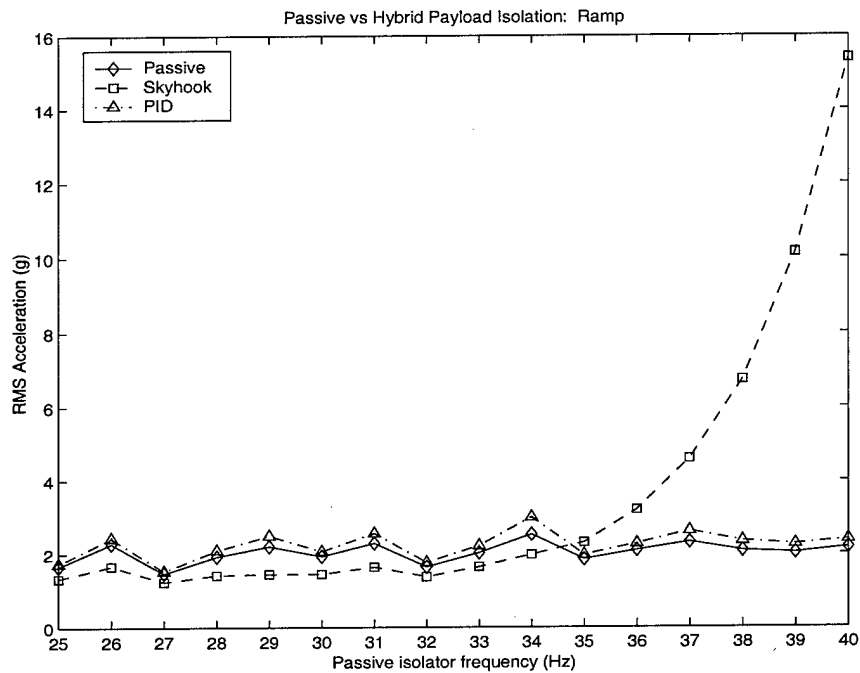
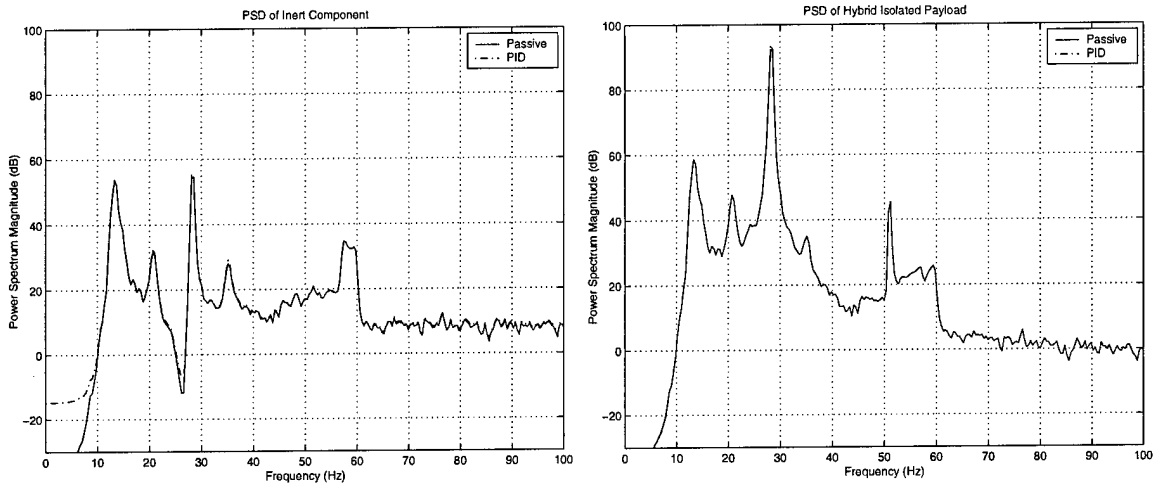


Figure 4.35 Active Control: RMS Acceleration vs. Isolator Frequencies, Ramp Resonant Burn

seems to show the best RMS acceleration reduction for isolator frequencies lower than 34 Hz. For isolator frequencies higher than 34 Hz, passive and PID active isolation exhibit similar performance, with a slight edge in favor of passive isolation.

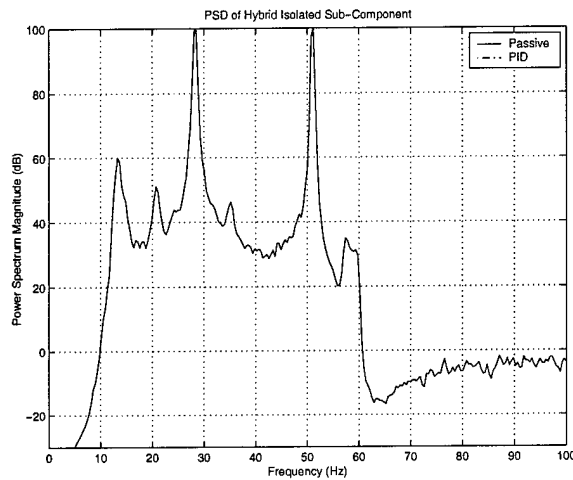
4.3.3.1 PID Control Results.

Figures 4.36 and 4.37 show the PSDs for the ramp resonant burn case. Although the 50 Hz resonant burn shows



(a) Inert Component Acceleration PSD

(b) Payload Acceleration PSD

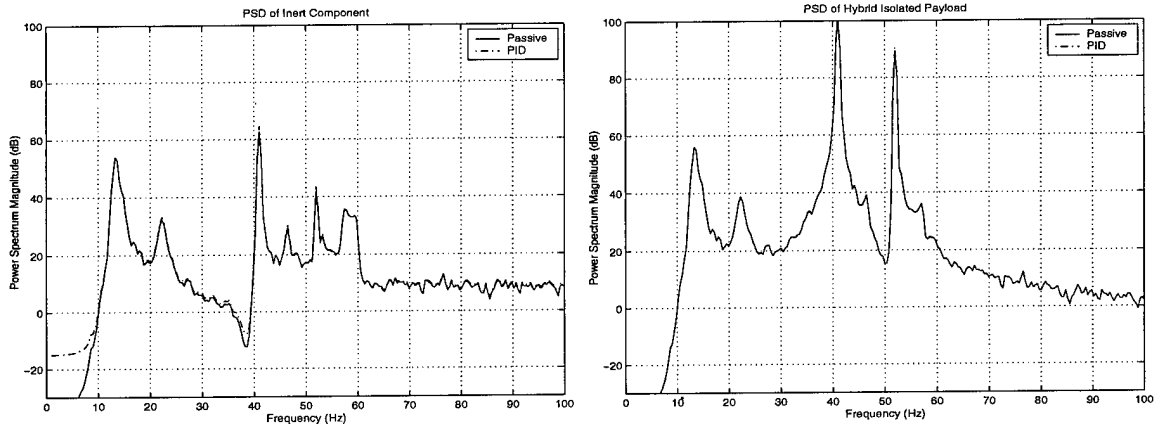


(c) Subcomponent Acceleration PSD

Figure 4.36 PID Control, 27 Hz Passive Isolator Inert Component, Payload, and Subcomponent Acceleration PSDs: Ramp Resonant Burn

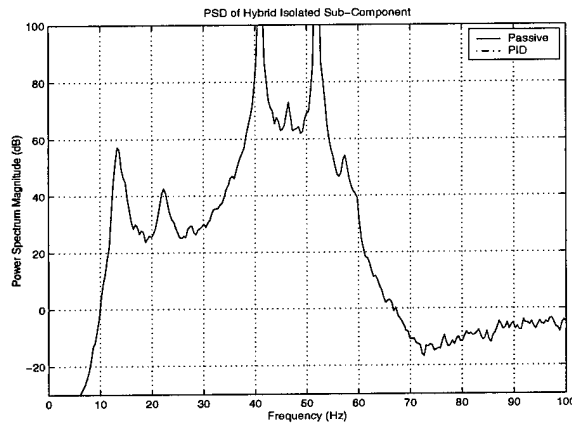
very little effect on the inert component, both the payload and the subcomponent show a substantial 50 Hz response. This is due to the natural frequency of the subcomponent interacting with the payload. The PID controller does very little

to reduce the magnitude of the isolator frequency response in both the 27 Hz case and the 40 Hz case. In general, the PID controller has very little effect on the low frequency vibrations of the payload.



(a) Inert Component Acceleration PSD

(b) Payload Acceleration PSD

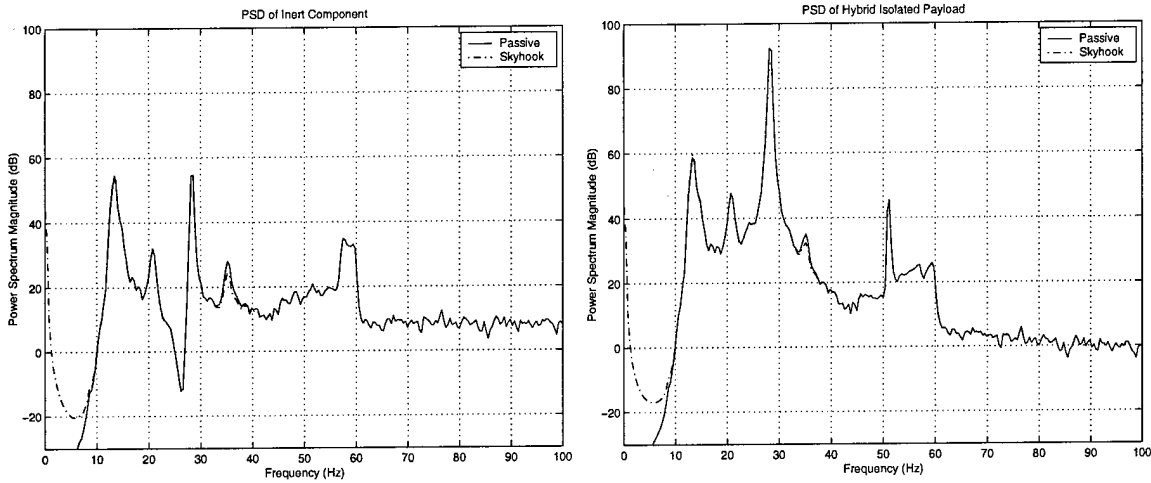


(c) Subcomponent Acceleration PSD

Figure 4.37 PID Control, 40 Hz Passive Isolator Inert Component, Payload, and Subcomponent Acceleration PSDs: Ramp Resonant Burn

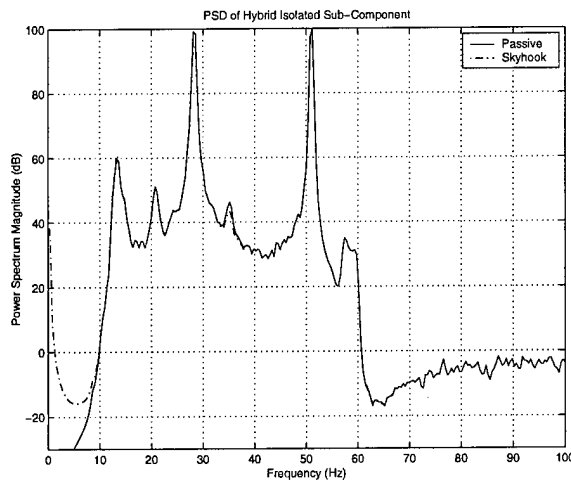
4.3.3.2 Skyhook Damper.

Like the PID controller, the skyhook damper does not show significant low frequency mode isolation or the ability to reduce the isolator mode without driving the launch vehicle unstable. However, unlike the PID controller, the isolation capability of the skyhook damper badly degrades at a passive isolator of 40 Hz (see Figures 4.38 and 4.39). The results for



(a) Inert Component Acceleration PSD

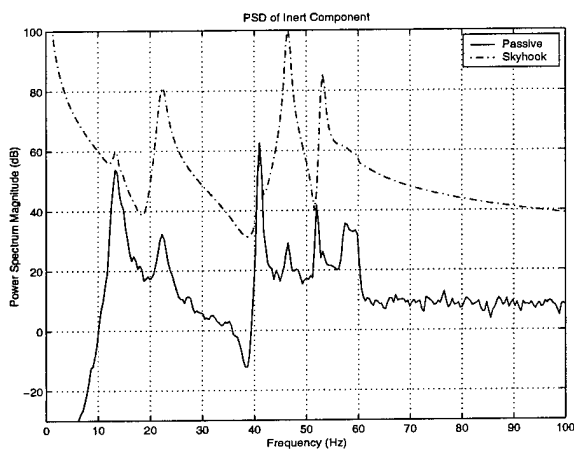
(b) Payload Acceleration PSD



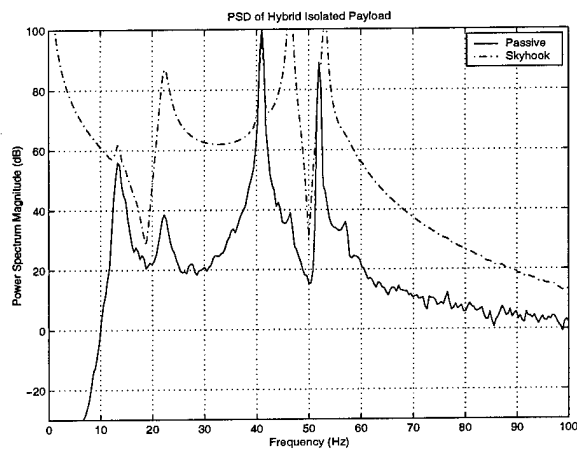
(c) Subcomponent Acceleration PSD

Figure 4.38 Skyhook Damper, 27 Hz Passive Isolator Inert Component, Payload, and Subcomponent Acceleration PSDs: Ramp Resonant Burn

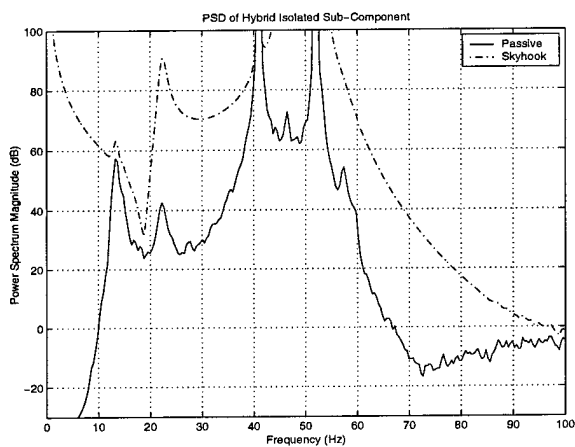
this ramp resonant burn case are similar to those of the fixed resonant burn case in Section 4.2.3.2. In the case of the ramp resonant burn, the payload's 50 Hz mode shown in both the 27 Hz and 40 Hz passive isolator cases is due to the vibration of the subcomponent rather than the resonant burn.



(a) Inert Component Acceleration PSD



(b) Payload Acceleration PSD

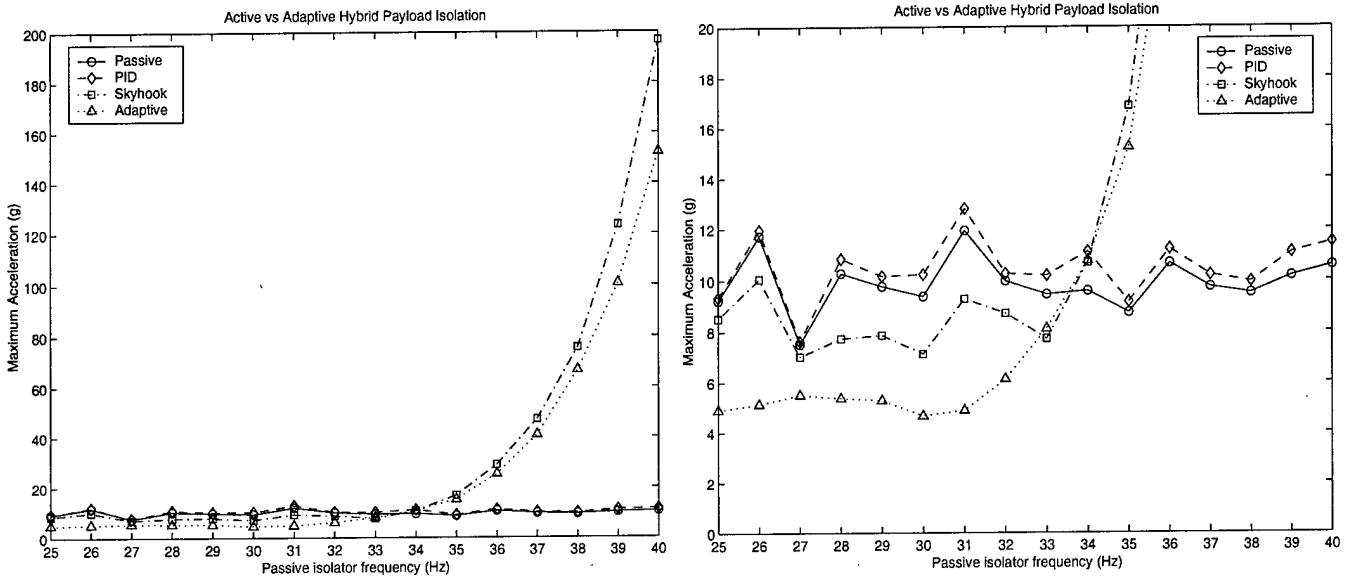


(c) Subcomponent Acceleration PSD

Figure 4.39 Skyhook Damper, 40 Hz Passive Isolator Inert Component, Payload, and Subcomponent Acceleration PSDs: Ramp Resonant Burn

4.3.4 Adaptive Control Results.

Figure 4.40 shows the maximum accelerations for the adaptively isolated payload with a ramp resonant burn. The results are again similar to those of the fixed resonant burn case. At



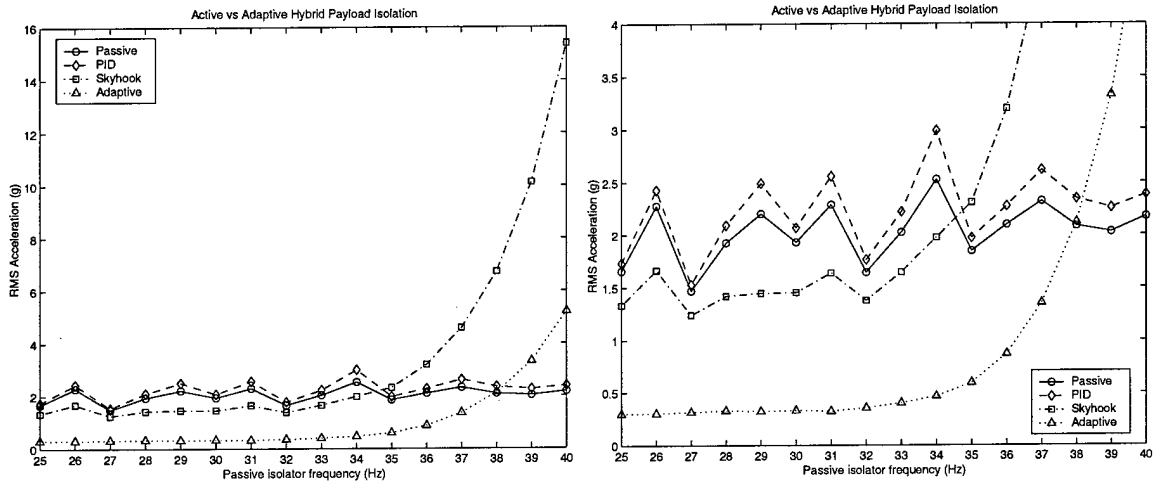
(a) Maximum Payload Accelerations

(b) Maximum Payload Accelerations (zoom)

Figure 4.40 Adaptive Control: Maximum Acceleration vs. Isolator Frequencies, Ramp Resonant Burn

approximately 34 Hz, the performance of the adaptive controller is severely degraded by the behavior of the subcomponent. The adaptive controller also shows benefits in significantly reducing maximum payload accelerations when used with a lower frequency passive isolator.

Figure 4.41 shows the RMS acceleration values for the resonant burn case using adaptive control. Again, adaptive vibration isolation shows a dramatic decrease in RMS acceleration for isolator frequencies below 38 Hz. At isolator frequencies above 38 Hz, the vibrations generated by the subcomponent dominate the behavior of the payload.

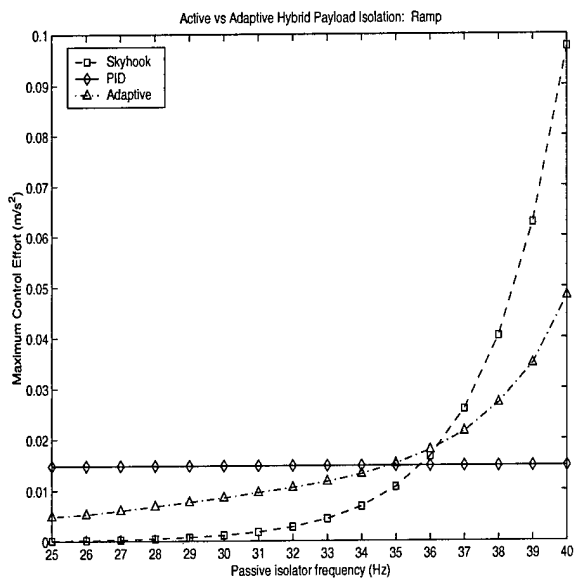


(a) RMS Payload Accelerations

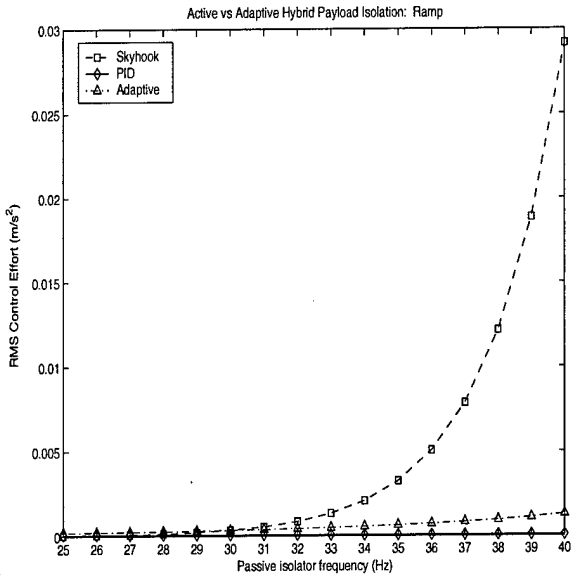
(b) RMS Payload Accelerations (zoom)

Figure 4.41 Adaptive Control: RMS Acceleration vs. Isolator Frequencies, Ramp Resonant Burn

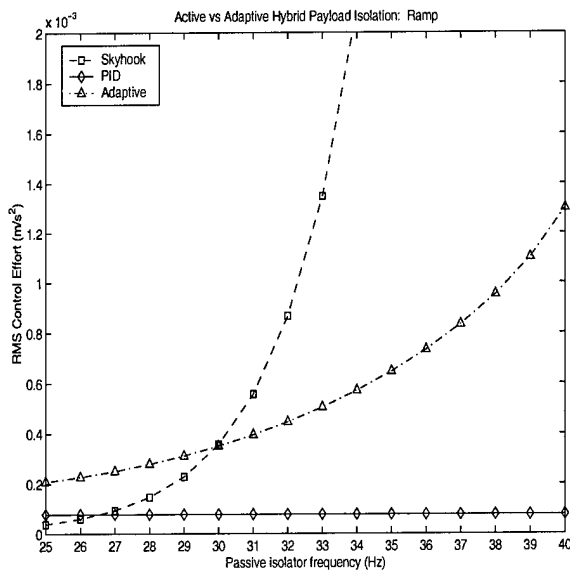
The ramp resonant burn case yields similar results to the fixed resonant burn case in terms of control effort expended (see Figure 4.42). Again, as was shown in Figure 4.25, the PID controller seems to require the least amount of control effort, while the skyhook damper and adaptive controller trade off differences in control effort. Also, the amount of control force required for the skyhook damper and the adaptive controller increases drastically as passive isolator approaches 50 Hz. The PID controller, however, yields poor modal control, though good RMS acceleration results over the range of passive isolator frequencies. This result is the same with the skyhook damper. The PSDs of the adaptive controller will help to investigate the modal control provided by the adaptive controller.



(a) Maximum Control Effort



(b) RMS Control Effort

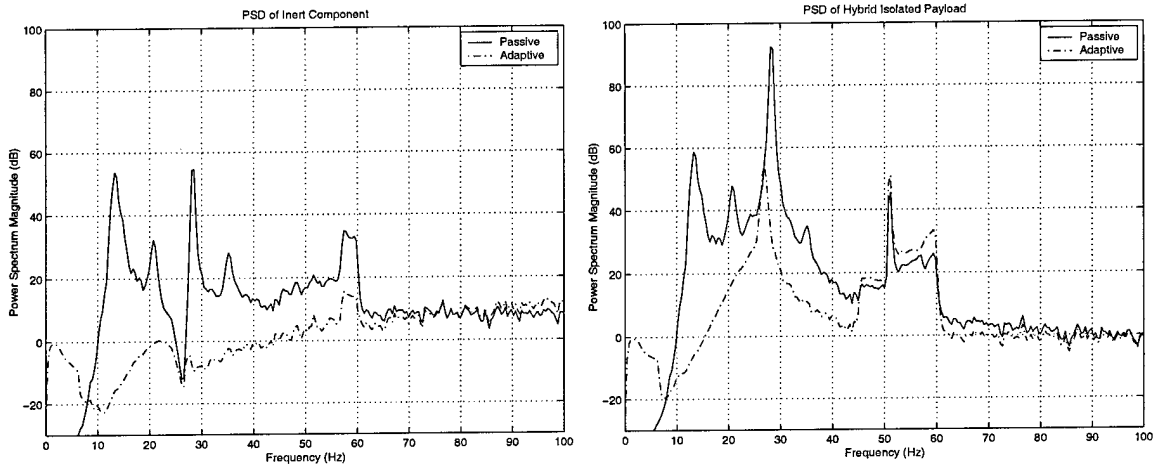


(c) RMS Control Effort (zoom)

Figure 4.42 Hybrid Control Effort: Ramp Resonant Burn

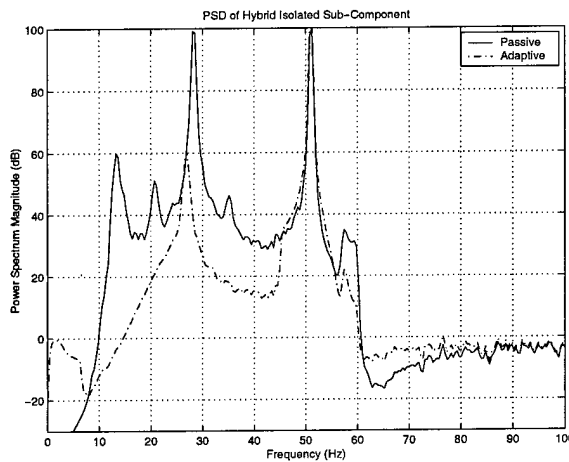
Looking at the PSDs for the adaptive controller (Figure 4.43 and Figure 4.44), it is clear that the adaptive controller is effective on the 10 Hz and 22 Hz launch vehi-

cle modes and the 27 Hz isolator mode. The adaptive controller effectively dampens



(a) Inert Component Acceleration PSD

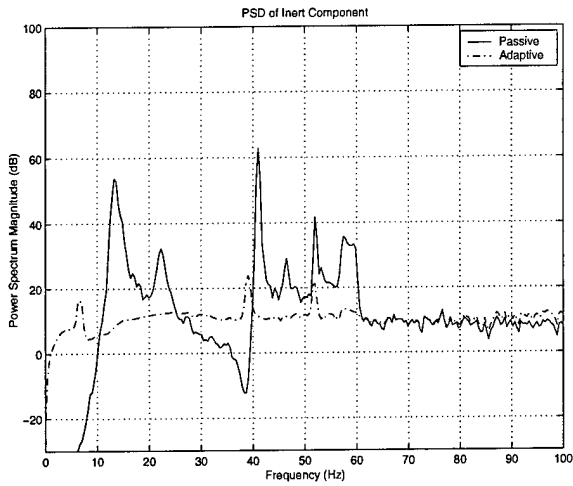
(b) Payload Acceleration PSD



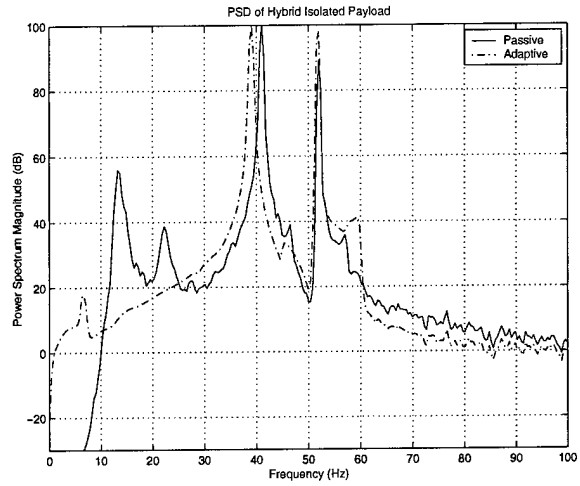
(c) Subcomponent Acceleration PSD

Figure 4.43 Adaptive Control, 27 Hz Passive Isolator Inert Component, Payload, and Subcomponent Acceleration PSDs: Ramp Resonant Burn

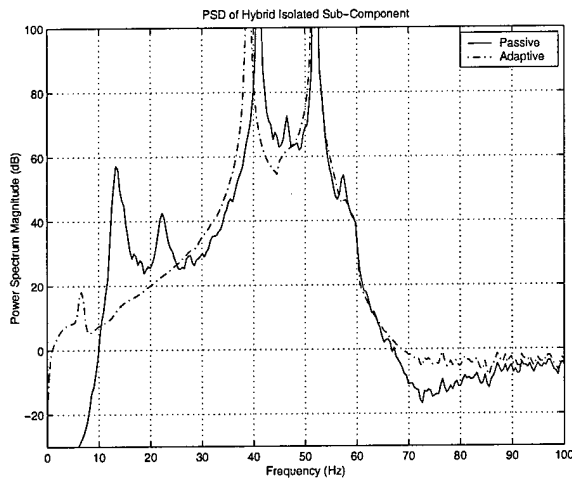
the inert component vibrations, thereby negating their effect on the payload. In the 40 Hz case, the adaptive controller is not able to attenuate the passive isolator mode because of its proximity to the natural frequency of the subcomponent. The vibrations of the subcomponent are not accounted for in the adaptive controller due to choosing the states of the subcomponent as being unmeasurable.



(a) Inert Component Acceleration PSD



(b) Payload Acceleration PSD



(c) Subcomponent Acceleration PSD

Figure 4.44 Adaptive Control, 40 Hz Passive Isolator Inert Component, Payload, and Subcomponent Acceleration PSDs: Ramp Resonant Burn

Dividing the model runs into a fixed resonant burn case and ramp resonant burn case clearly showed the effect that the subcomponent can have on the payload during launch. For both resonant burn cases, the PID controller gave consistent results across all passive isolator frequencies, while both the skyhook damper and adaptive controller could not dampen the vibrations of the subcomponent when the passive isolator frequency approached the subcomponent natural frequency. For the lower passive isolator frequency, the adaptive controller shows as much as a ninety percent improvement over the passive-only or active hybrid isolators.

V. Findings, Conclusions and Recommendations

5.1 Summary of Findings and Conclusions

All hybrid vibration isolators behaved differently at various passive isolator frequencies. The skyhook damper and the adaptive isolator both showed degradation in performance as the passive isolator's frequency approached the natural frequency of the subcomponent. The ramp resonant burn cases show that the subcomponent drives the payload vibration more than the resonant burn frequency. When designing the payload, the amount of damping on the subcomponent may be a critical parameter if one subcomponent can drive the vibrations of the payload.

The PID controller showed favorable payload vibration isolation over all passive isolator frequencies. The PID controller is not modeled as a structure, and therefore is not as adversely affected by resonances as the skyhook damper and adaptive isolator. Although it did not produce lower maximum and RMS acceleration results than the skyhook damper, it is more effective when the passive isolator frequency is near the natural frequency of the subcomponent. In contrast, the PID controller showed poor modal control in trying to reduce the response of specific payload modes. In general, the PID controller does very little to reduce low frequency modes, while it does produce favorable results over the full range of frequencies.

The skyhook damper targeted the passive isolator mode, but was not able to significantly reduce this response. Different from a traditional skyhook damper, in this model it was not attached to an inertial base, but to the vibrating inert component of the launch vehicle. The skyhook damper actually interacted with the passive isolator and vibrations of the inert component in order to reduce the maximum and RMS accelerations of the payload.

The adaptive vibration isolator treated the vibrations of the inert component as controllable and observable, while the subcomponent vibrations were left as unmeasurable. The adaptive isolator suppressed inert component vibration. The subcomponent, mainly affected by the passive isolator, affects the payload more adversely than with the PID controller or just passive isolation at passive isolator frequencies near the subcomponent natural frequency. In order to isolate the payload from the subcomponent, subcomponent damping must be taken into consideration or the subcomponent vibration needs to be a measurable state.

5.2 Recommendations

Since the subcomponent seemed to drive a mode in the payload vibration, the effects of increased subcomponent damping and corresponding stiffness should be investigated. Although changing the mass of the subcomponent seemed to show little effect, the interaction between the passive isolator and subcomponent should be studied. Further, this interaction coupled with the modal effects of active and adaptive control should be researched.

The PID control force seemed to remain constant over the range of passive isolator frequencies. This phenomenon should be investigated over a wider range of frequencies to see if the PID controller actually behaves independently of passive isolator frequency or if there are limits on the PID controller's performance. The PID gains should also be varied to reveal their effects on maximum and RMS payload acceleration and on the amount of control effort expended.

The skyhook damper could not significantly reduce the isolator mode in the payload vibrations without driving the entire launch vehicle unstable. Since it transmitted force to the inert component, the controller damping and stiffness should be investigated to reveal stability and performance limits.

The adaptive controller showed the best performance at low isolator frequencies, however it could not perform effectively at passive isolator frequencies near the subcomponent natural frequency. Several model runs should be used to reveal the effects of a measurable subcomponent. This effect on the amount of control effort needed should also be researched.

Both of the active isolators and the adaptive isolator yielded favorable results and increased performance over a passive isolator. The hybrid isolators also show clear interaction with the passive isolation of the payload. In order to address the feasibility of using these hybrid isolators, their interaction with the rest of the launch vehicle needs to be more clearly understood.

Bibliography

1. Argento, James M. *Vibration Isolation Modeling for Launch Vehicle Payloads*. MS thesis, Vanderbilt University, May 1993.
2. Burdisso, R.A. and J.D. Heilmann. "A New Dual-Reaction Mass Dynamic Vibration Absorber Actuator for Active Vibration Control," *Journal of Sound and Vibration*, 214(5):817-831 (1998).
3. Edberg, D.L. *Launch Vibration Isolation System*. Technical Report PL-TR-97-1086, Kirtland AFB, NM: Phillips Laboratory, April 1997.
4. Elliott, Stephen J., et al. "A Multiple Error LMS Algorithm and its Application to the Active Control of Sound and Vibration," *IEEE Transactions on Acoustics, Speech, and Signal Processing*, ASSP-35(10):1423-1434 (October 1987).
5. Ertur, David, et al. "Adaptive Vibration Isolation for Flexible Structures," *Journal of Vibrations and Acoustics*, 121:440-445 (October 1999).
6. Franklin, Gene F., et al. *Feedback Control*. New York: Addison-Wesley, 1994.
7. Fuller, C. R., et al. *Active Control of Vibration* (1 Edition). Academic Press, 1996.
8. Fuller, C.R. and A.H. von Flotow. "Active Control of Sound and Vibration," *IEEE Control Systems Magazine*, 15(6):9-19 (December 1995).
9. Goh, C.J. and T.K. Caughey. "On the Stability Problem Caused by Finite Actuator Dynamics in the Collocated Control of Large Space Structures," *International Journal of Control*, 41(3):787-802 (1985).
10. Guigou, C., et al. "Active Isolation of Vibration with Adaptive Structures," *Journal of the Acoustical Society of America*, 96(1):294-299 (July 1994).
11. Hillerström, Gunnar. "Adaptive Suppression of Vibrations - A Repetitive Control Approach," *IEEE Transactions on Control Systems Technology*, 4(1):72-78 (January 1996).
12. Inman, Daniel J. *Engineering Vibration*. Englewood Cliffs, New Jersey: Prentice-Hall, Inc., 1994.
13. Johnson, Conor D., et al. "Whole-Spacecraft Vibration Isolation System for the GFO/Taurus Mission," *SPIE Conference on Passive Damping*, 3672:175-185 (March 1999).
14. Karahalidis, Gregory G. *Whole Spacecraft Vibration Isolation*. MS thesis, Air Force Institute of Technology, March 1999.

15. Karnopp, D. "Active and Semi-Active Vibration Isolation," *Transactions of the ASME*, 117:177-185 (June 1995).
16. Larson, T.W. and J.M Newell. "Test Philosophies for the New Millennium," *Journal of the Institute of Environmental Sciences*, 40(3):22-27 (1997).
17. Lee-Glauser, Gina J., et al. "Satellite Active and Passive Vibration Control During Liftoff," *Journal of Spacecraft and Rockets*, 33(3):428-432 (May-June 1996).
18. Mangiante, Gérard and Alain Roure. "Compact Multichannel Controller for Active Noise and Vibration Control," *Noise Control Engineering Journal*, 43(2):43-50 (March-April 1995).
19. Meirovitch, Leonard. *Elements of Vibration Analysis* (2 Edition). McGraw Hill, 1986.
20. Queiroz, M.S., et al. "Adaptive Vibration Control of an Axially Moving String," *Journal of Vibration and Acoustics*, 121:41-49 (January 1999).
21. Reid, J. Gary. *Linear System Fundamentals: Continuous and Discrete, Classic and Modern*. New York: McGraw-Hill, Inc., 1983.
22. Salemi, P., et al. "Active Control of Forced and Unforced Structural Vibration," *Journal of Sound and Vibration*, 208(1):15-32 (1997).
23. Sciulli, Dino. *Dynamics and Control for Vibration Isolation*. PhD dissertation, Virginia Polytechnic and State University, April 1997.
24. Sciulli, Dino and Steve Griffin. "Hybrid Launch Isolation System," *The 6th SPIE Smart Structures and Materials Conference*, 1-8 (1999).
25. Sciulli, Dino and Daniel J. Inman. "Comparison of Single- and Two-Degree-of-Freedom Models for Passive and Active Vibration Isolation Design," *Smart Structures and Materials 1996: Passive Damping and Isolation*, 2720:293-304 (1996).
26. Sievers, Lisa A. and Andreas H. von Flotow. "Linear Control Design for Active Vibration Isolation and Narrow Band Disturbances," *Proceedings of the 27th Conference on Decision and Control*, 3:1032-1037 (1988).
27. Sievers, Lisa A. and Andreas H. von Flotow. "Comparisons and Extensions of Control Methods for Narrow-Band Disturbance Rejection," *IEEE Transactions on Signal Processing*, 40(10):2377-2391 (October 1992).
28. Sievers, Lisa A., et al. "Isolation of a Vibrating Machine Mounted on a Flexible Structure," *Proceedings of the American Control Conference*, 2:1182-1188 (June 1989).

29. Spanos, J., et al. "Active Vibration Isolation on an Experimental Space Structure," *Proceedings of the SPIE - Smart Structures and Intelligent Systems*, 674-680 (February 1993).
30. Tanner, Carole S. "Lessons Learned in Predicting Launch Vehicle Vibroacoustic Environments," *Journal of the Institute of Environmental Sciences*, 38-42 (March 1997).
31. Timmins, A. R. *A Study of First-Day Space Malfunctions*. Technical Note D-6464, NASA, 1974.
32. Timmins, A. R. *A Study of First-Month Space Malfunctions*. Technical Note D-7750, NASA, 1974.
33. von Flotow, A.H. "An Expository Overview of Active Control and Machinery Mounts," *Proceedings of the 27th Conference on Decision and Control*, 3:2029-2032 (December 1988).

Vita

Julian Roman Jarosh was born on January 5th, 1973 in Philadelphia, PA. He grew up in Queensbury, NY, on the southern border of Adirondack Park. There, he attended Queensbury High School and graduated with honors. In June, 1991, he began Basic Training at the United States Air Force Academy. On May 31st, 1995 he received his Bachelor of Science degree in Astronautical Engineering from the Air Force Academy. He graduated with academic distinction and a minor in French. On May 31st, 1998, he received his Master of Business Administration degree specializing in Technology Management from the University of Phoenix while stationed at Kirtland Air Force Base, New Mexico. Upon completion of the Master's Degree program at the Air Force Institute of Technology, Wright-Patterson AFB, Ohio, Capt Jarosh will be assigned to the 2nd Space Operations Squadron, Schriever AFB, Colorado.

Permanent address: 8 Crownwood Lane
Queensbury, NY 12804

REPORT DOCUMENTATION PAGE			Form Approved OMB No. 0704-0188	
Public reporting burden for this collection of information is estimated to average 1 hour per response, including the time for reviewing instructions, searching existing data sources, gathering and maintaining the data needed, and completing and reviewing the collection of information. Send comments regarding this burden estimate or any other aspect of this collection of information, including suggestions for reducing this burden, to Washington Headquarters Services, Directorate for Information Operations and Reports, 1215 Jefferson Davis Highway, Suite 1204, Arlington, VA 22202-4302, and to the Office of Management and Budget, Paperwork Reduction Project (0704-0188), Washington, DC 20503.				
1. AGENCY USE ONLY (Leave blank)	2. REPORT DATE 9 Mar 00	3. REPORT TYPE AND DATES COVERED Master's Thesis		
4. TITLE AND SUBTITLE ACTIVE AND ADAPTIVE CONTROL FOR PAYLOAD LAUNCH VIBRATION ISOLATION			5. FUNDING NUMBERS	
6. AUTHOR(S) Julian R. Jarosh, Captain USAF				
7. PERFORMING ORGANIZATION NAME(S) AND ADDRESS(ES) Air Force Institute of Technology 2950 P Street Wright-Patterson AFB, OH 45433-7765			8. PERFORMING ORGANIZATION REPORT NUMBER AFIT/GA/ENY/00M-03	
9. SPONSORING/MONITORING AGENCY NAME(S) AND ADDRESS(ES) AFRL/VSDV 3550 Aberdeen Avenue SE Kirtland AFB, NM 87117-5776			10. SPONSORING/MONITORING AGENCY REPORT NUMBER	
11. SUPPLEMENTARY NOTES Capt Gregory S. Agnes, PhD (937) 255-6565 x4317 Gregory.Agnes@afit.af.mil				
12a. DISTRIBUTION AVAILABILITY STATEMENT APPROVED FOR PUBLIC RELEASE; DISTRIBUTION UNLIMITED			12b. DISTRIBUTION CODE	
13. ABSTRACT (Maximum 200 words) The Department of Defense has identified launch vibration isolation as a major research interest. Reducing the loads a satellite experiences during launch will greatly enhance its reliability and lifetime, and reduce payload structural mass. DoD space programs stand to benefit significantly from advances in vibration isolation technology. This study explores potential hybrid vibration isolation using active and adaptive control with a passive vibration isolator. The active control methods are Porportional-Integral-Derivative (PID) control and a skyhook damper. Lyapunov analysis is used to develop the structural adaptive control scheme. Simulink and Matlab simulations investigate these control methodologies on a lumped mass dynamic model of a satellite and its representative launch vehicle. The results of the modeling indicate adaptive control achieves up to a 90 percent reduction in loads on the payload when compared to the conventional active control methods. The adaptive controller compensated for the loads being transmitted to the payload from the rest of the launch vehicle. The current adaptive controller was not able to effectively control the motion of a vibrating subcomponent within the payload or the subcomponent's effect on the overall payload itself.				
14. SUBJECT TERMS Vibration Isolation, Active Control, Adaptive Control, Launch Vehicle, Satellite, Spacecraft, Vibration, Launch Environment, Isolation, Suppression			15. NUMBER OF PAGES 99	
			16. PRICE CODE	
17. SECURITY CLASSIFICATION OF REPORT UNCLASSIFIED	18. SECURITY CLASSIFICATION OF THIS PAGE UNCLASSIFIED	19. SECURITY CLASSIFICATION OF ABSTRACT UNCLASSIFIED	20. LIMITATION OF ABSTRACT UL	